Neuron

Article

Non-canonical glutamate signaling in a genetic model of migraine with aura

Highlights

- FHM2 knockin mice have "plumes" of glutamate release in the cortex
- Plumes are a consequence of inefficient glutamate clearance
- A flurry of plumes precedes the onset of spreading depolarization at its origin
- Spreading depolarization itself induces plumes as it propagates through the cortex

Authors

Patrick D. Parker, Pratyush Suryavanshi, Marcello Melone, ..., C. William Shuttleworth, Daniela Pietrobon, K.C. Brennan

Correspondence

daniela.pietrobon@unipd.it (D.P.), k.c.brennan@hsc.utah.edu (K.C.B.)

In Brief

Migraine is a common and debilitating neurological disorder whose underlying neurobiology is poorly understood. Parker et al. report "plumes" of glutamate release in a genetic model of migraine that are a consequence of inefficient glutamate clearance. Plumes also precede the onset of spreading depolarization, the physiological correlate of migraine aura.

Parker et al., 2021, Neuron *109*, 611–628
February 17, 2021
https://doi.org/10.1016/j.neuron.2020.11.018

CellPress

Neuron

CellPress
OPEN ACCESS

Article

Non-canonical glutamate signaling in a genetic model of migraine with aura

Patrick D. Parker,[1,2] Pratyush Suryavanshi,[1,2,9] Marcello Melone,[3,4,9] Punam A. Sawant-Pokam,[1] Katelyn M. Reinhart,[1,6] Dan Kaufmann,[1] Jeremy J. Theriot,[1] Arianna Pugliese,[3] Fiorenzo Conti,[3,4,5] C. William Shuttleworth,[6] Daniela Pietrobon,[7,8,*] and K.C. Brennan[1,10,*]

[1]Department of Neurology, University of Utah School of Medicine, Salt Lake City, UT 84108, USA
[2]Interdepartmental Program in Neuroscience, University of Utah School of Medicine, Salt Lake City, UT 84108, USA
[3]Section of Neuroscience and Cell Biology, Department of Experimental and Clinical Medicine, Università Politecnica delle Marche, Ancona 60020, Italy
[4]Center for Neurobiology of Aging, IRCCS INRCA, Ancona 60020, Italy
[5]Foundation for Molecular Medicine, Università Politecnica delle Marche, Ancona 60020, Italy
[6]Department of Neurosciences, University of New Mexico School of Medicine, Albuquerque, NM 87106, USA
[7]Department of Biomedical Sciences and Padova Neuroscience Center (PNC), University of Padova, 35131 Padova, Italy
[8]CNR Institute of Neuroscience, 35131 Padova, Italy
[9]These authors contributed equally
[10]Lead contact
*Correspondence: daniela.pietrobon@unipd.it (D.P.), k.c.brennan@hsc.utah.edu (K.C.B.)
https://doi.org/10.1016/j.neuron.2020.11.018

SUMMARY

Migraine with aura is a common but poorly understood sensory circuit disorder. Monogenic models allow an opportunity to investigate its mechanisms, including spreading depolarization (SD), the phenomenon underlying migraine aura. Using fluorescent glutamate imaging, we show that awake mice carrying a familial hemiplegic migraine type 2 (FHM2) mutation have slower clearance during sensory processing, as well as previously undescribed spontaneous "plumes" of glutamate. Glutamatergic plumes overlapped anatomically with a reduced density of GLT-1a-positive astrocyte processes and were mimicked in wild-type animals by inhibiting glutamate clearance. Plume pharmacology and plume-like neural Ca^{2+} events were consistent with action-potential-independent spontaneous glutamate release, suggesting plumes are a consequence of inefficient clearance following synaptic release. Importantly, a rise in basal glutamate and plume frequency predicted the onset of SD in both FHM2 and wild-type mice, providing a novel mechanism in migraine with aura and, by extension, the other neurological disorders where SD occurs.

INTRODUCTION

Migraine with aura is a common and debilitating neurological disorder, consisting of severe head pain and sensory amplifications. For a third of migraineurs, the headache is preceded by an aura, which most commonly is a spreading sensory hallucination (flashing visual percepts, numbness, and tingling) (Brennan and Pietrobon, 2018). The aura is useful for investigative purposes because it is known to be caused by a spreading depolarization (SD) of brain tissue (also known as cortical spreading depression) that can be induced and measured experimentally. SD also initiates headache mechanisms in animal models (Burstein et al., 2015; Pietrobon and Moskowitz, 2014) and is thus the earliest physiologically measurable feature of the migraine attack. Monogenic forms of migraine have been used to generate mouse models, and despite mechanistically diverse mutations, thus far all models show an increased susceptibility to SD (Brennan et al., 2013; Capuani et al., 2016; Eikermann-Haerter et al., 2009, 2011; Jansen et al., 2020; Leo et al., 2011; van den Maagdenberg et al., 2004, 2010; Tottene et al., 2009).

Familial hemiplegic migraine type 2 (FHM2) is a form of migraine with aura that arises from loss-of-function mutations to *ATP1A2*, the gene encoding the predominantly astrocytic α2 Na^+/K^+-ATPase (α2NKA) (De Fusco et al., 2003; Pietrobon, 2007). Heterozygous FHM2 "knockin" mice (*Atp1a2*$^{+/W887R}$; the homozygous mutation is lethal) express roughly half of the α2NKA protein that is expressed in wild-type (WT) animals (Leo et al., 2011). They also show a ~50% reduction in the glutamate transporter GLT-1a in perisynaptic astrocyte processes relative to WT (Capuani et al., 2016). This is likely because α2NKA colocalizes with glutamate transporters in astrocyte processes and may be physically coupled to them as part of a macromolecular complex (Cholet et al., 2002; Melone et al., 2019; Rose et al., 2009). Consequently, FHM2 astrocytes show slower uptake kinetics of glutamate and K^+ following synaptic activity (Capuani et al., 2016). Astrocyte glutamate uptake is critical for

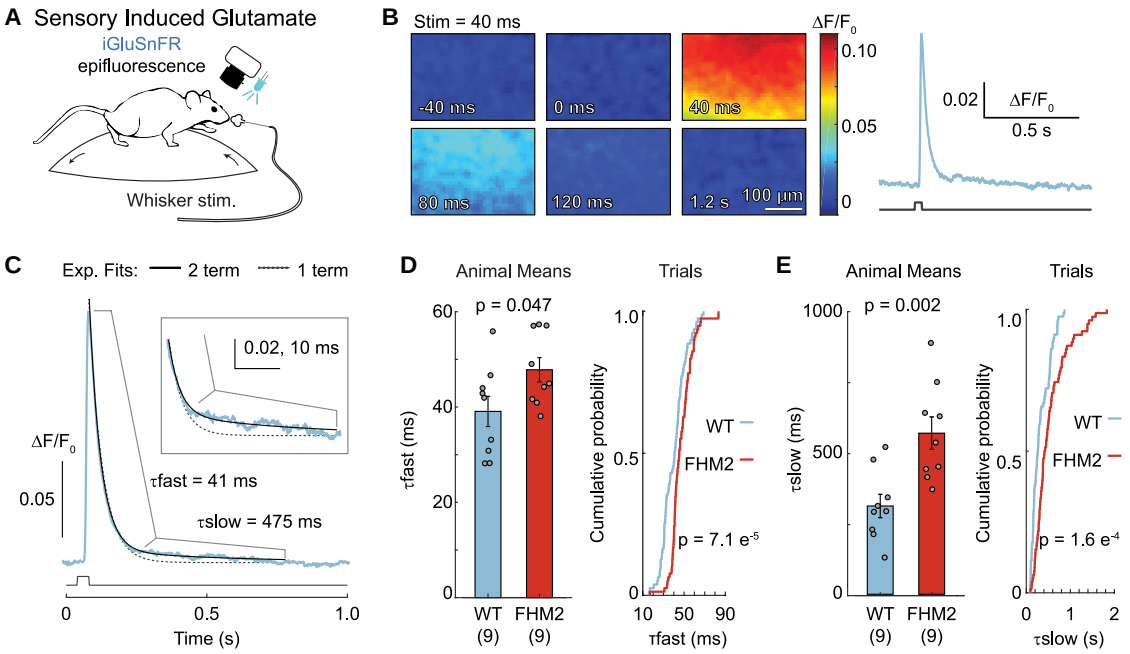

Figure 1. Slowed glutamate clearance in awake FHM2 mice

(A) Fluorescent glutamate imaging was performed in awake, head-fixed mice by using epifluorescence combined with whisker stimulation.

(B) Fluorescent glutamate response (left) in the barrel cortex following a 40-ms whisker stimulation (at 0 ms) with quantification (right).

(C) Glutamate clearance rates were determined by fitting the decay of the glutamate response with a 2-term exponential equation (black solid line; blue, glutamate fluorescence from a single trial; dashed line, single-term fit). Boxed inset: magnification of the trace to illustrate poor fit of a single-term equation.

(D and E) Glutamate clearance kinetics for τ_{fast} (D) and τ_{slow} (E). Means, two-sample t test; n = 9 mice/group. Trials, 2-sample Kolmogorov-Smirnov; n = 79 trials for WT and 78 for FHM2. Error bars represent SEM.

See also Figure S1.

maintaining the temporal and spatial characteristics of excitatory neurotransmission (Bergles and Jahr, 1997; Danbolt, 2001; Diamond and Jahr, 1997; Rothstein et al., 1996; Tanaka et al., 1997), but how this astrocytic mutation reshapes glutamate signaling in awake FHM2 mice is largely unknown.

To measure glutamate signaling under disease-relevant conditions, we recorded it in awake animals using the fluorescent glutamate reporter iGluSnFR (Marvin et al., 2013). We found that FHM2 mice have slowed glutamate clearance following sensory stimulation, as well as previously undescribed "plumes" of glutamate that occurred spontaneously in FHM2 mice, and correlated with the initiation of SD in both WT and FHM2 mice. Moreover, we found SD itself induced plumes as it propagated away from the initiation site, illustrating continued glutamate release and uptake dysregulation following the depolarizing wavefront. Our results thus reveal a new mechanism not only for migraine but also potentially for other disorders in which SD occurs.

RESULTS

Glutamate clearance is slowed during sensory processing in FHM2 mice

We used fast (500 Hz) epifluorescence imaging with iGluSnFR (expressed on neurons using the synapsin-1 promoter) to measure glutamate responses in the barrel cortex of awake, head-fixed FHM2 mice and WT littermates (Figure 1A). Unilateral puffs of air (40 ms; 40 psi; deflecting all whiskers) increased glutamate fluorescence over a large region of the barrel cortex (360 × 250 µm) (Figure 1B). Clearance rates were determined by fitting a 2-term exponential to the decay of the response (initial τ_{fast} followed by a second τ_{slow}; see STAR methods) (Figure 1C). Decay kinetics were slower in FHM2 mice than in WT littermates (~22% change for τ_{fast} and ~82% for τ_{slow}) (Figures 1D and 1E). There was no difference in the slope of the rise of the glutamate response between the 2 genotypes (Figure S1A). These results, showing impaired glutamate clearance using an ethologically and disease-relevant stimulus in awake animals, provide support for a proposed mechanism of the FHM2 mutation (Capuani et al., 2016).

Spontaneous non-canonical glutamate signaling—glutamatergic plumes—in awake FHM2 mice

In addition to the spatially broad whisker-induced response, we observed more focal, higher-amplitude glutamate fluorescence events under 2-photon microscopy (Figures 2 and S1; Videos S1 and S2). These previously uncharacterized glutamatergic plumes were generally circular in nature, appeared to spread from a central origin (Figures 2A, 2C, and S1C–S1E), and were observed in the absence of sensory stimulation (Figure S1G). Plumes frequently occurred during baseline recordings in FHM2 mice but were quite rare in WT mice (Figures 2D and

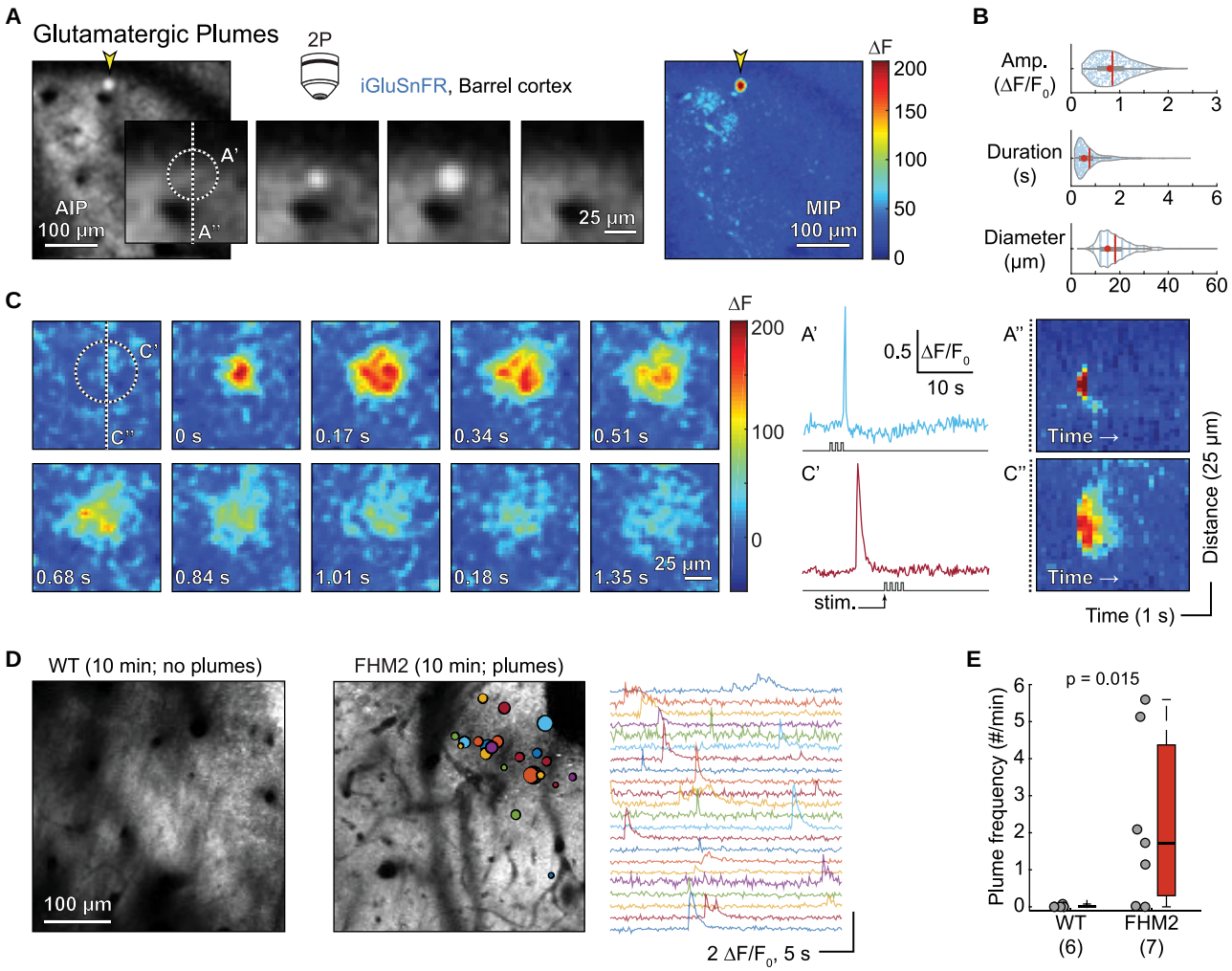

Figure 2. Glutamatergic plumes in awake FHM2 mice

(A) Example of a plume (yellow arrowhead) in a FHM2 mouse measured using 2-photon microscopy (2P). Center panels: magnified view of the plume over time (169 ms/panel). AIP, average intensity projection. Raw images with a Gaussian blur (see STAR Methods). Right: maximum intensity projection (MIP) of change in fluorescence (ΔF) over the entire stimulation trial (33.78 s) illustrates amplitude of the plume relative to all other glutamate signaling.

(B) Amplitude (Amp.; top; $\Delta F/F_0$), duration (middle; s), and diameter (bottom; µm) of n = 590 plumes from 7 FHM2 mice. Red circle, median; vertical line, mean.

(C) Example of a second plume with longer duration and larger diameter than that in (A). Panels are successive imaging frames, starting at the top left corner and ending at the bottom right.

(A′ and C′) Quantification of the two plumes. Note that plumes occurred during and outside of whisker stimulation (stim.).

(A′′ and C′′) Kymographs illustrate that both plumes started at a central location and expanded with time. Colorbar as in (A) and (C).

(D) AIP from a WT (left) and a FHM2 (right) mouse with colored circles overlaid to indicate location and size of plumes, as well as corresponding traces. WT is representative of their general lack of plumes under baseline conditions.

(E) Frequency of plumes by genotype (Wilcoxon rank-sum test; n, number of mice in parentheses). For all figures, "box whisker" represents the median (horizontal line), interquartile range (IQR; "box"), 1.5 × IQR ("whiskers"), and >1.5 × IQR ("+").

See also Figure S1, and Videos S1 and S2.

2E). The average (± standard deviation) frequency of plumes was 2.74 ± 1.86 plumes/minute, and the average duration was 743 ± 620 ms, with many events lasting longer than 1 s in FHM2 mice (Figure 2B; Data S1), suggesting a potential breakdown in glutamate clearance mechanisms. Importantly, plumes were observed in thin skull experiments, showing that they were not caused by removing the skull during craniotomy (Figures S2E and S2I).

Glutamatergic plumes are a consequence of inefficient glutamate clearance

Plumes occurred predominantly in superficial cortical layer 1 (putative L1a) (Vogt, 1991) and much less frequently in deeper L1b and L2/3 (Figures 3A and 3B). We labeled astrocytes with SR101 *in vivo* (Nimmerjahn and Helmchen, 2012) and observed a reduced incidence of astrocyte somas up to ~15–30 µm below the glia limitans in WT and FHM2 mice, confirming a previous

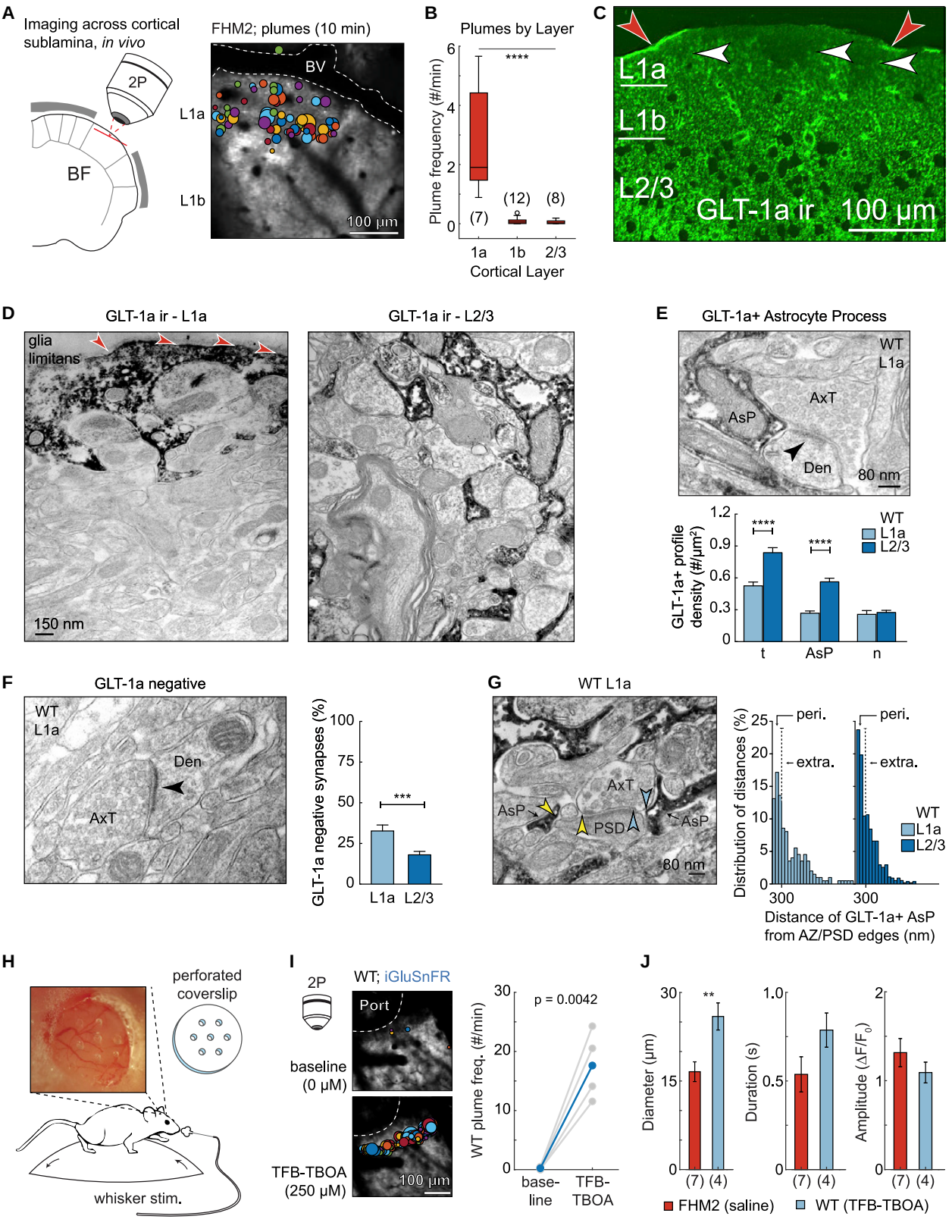

(legend on next page)

report using this method (McCaslin et al., 2011; Figures S2A and S2D). In a separate set of experiments, we observed irregular areas of reduced GLT-1a immunofluorescence in L1a, compared to adjacent tissue within the same layer and compared to deeper L1b and L2/3 (Figures 3C and S2B).

These combined results suggested that L1a may be predisposed to plumes due to reduced coverage of glutamatergic synapses by perisynaptic astrocyte processes. We tested this hypothesis using pre-embedded electron microscopy with immunoreactivity for GLT-1a, which labeled astrocyte processes as well as some axons (Melone et al., 2009, 2011, 2019). This method confirmed a significantly lower GLT-1a immunoreactivity in the neuropil of L1a compared to L2/3 and a high incidence of immunoreactivity in the glia limitans (Figures 3D and S2C). In both WT and FHM2 mice, L1a had a reduced density of GLT-1a+ astrocyte processes compared to L2/3 (Figures 3E and S2E) and a larger proportion of asymmetric (putative excitatory) synapses lacking GLT-1a immunoreactivity entirely (Figures 3F and S2F). For asymmetric synapses with adjacent GLT-1a+ astrocyte processes, we measured the distance from the edges of the presynaptic active zone and postsynaptic density to the closest astrocyte process. L1a contained a lower proportion of perisynaptic astrocyte processes (<300 nm) and a larger proportion of extrasynaptic processes (>300 nm) than L2/3 (Melone et al., 2009, 2011, 2019; Figures 3G and S2G), indicating a greater distance of astrocyte processes from the primary glutamate release site. This synaptic architecture suggests an anatomical influence on plume incidence, mediated by reduced glutamate clearance capabilities in L1a.

We hypothesized that the frequent presence of plumes in L1a of FHM2 but not WT mice might be due to the known impairment of glutamate uptake by astrocytes in FHM2 mice (Capuani et al., 2016). If this were the case, we should be able to replicate the FHM2 phenotype in WT mice by inhibition of glutamate uptake. Indeed, we observed a high frequency of plumes in L1a following superfusion of the glutamate transporter inhibitor (3S)-3-[[3-[[4-(trifluoromethyl)benzoyl]amino]phenyl]methoxy]-L-aspartic acid (TFB-TBOA) through a perforated coverslip in awake WT mice (Figures 3H–3J). This result suggests that the presence of spontaneous plumes in L1a in FHM2 mice is due to a combined paucity of GLT-1a+ astrocyte processes relative to deeper layers and an impaired rate of glutamate uptake by individual astrocytes.

The frequency and diameter of TFB-TBOA-induced plumes in WT mice *in vivo* were greater than those observed for spontaneous events in FHM2, which we hypothesized was due to a greater inhibition of clearance by TFB-TBOA than the FHM2 mutation. Consistent with this finding, experiments in slices from the barrel cortex showed a dose response of plume incidence, size, and duration to increasing TFB-TBOA concentration in FHM2 mice (Figures S3A–S3E). Taken together, these experiments show that the plumes described here are a consequence of impaired glutamate uptake, that they are not necessarily a unique characteristic of FHM2 mice, and that they might arise under different conditions in which glutamate uptake is compromised.

Glutamate release during plumes is consistent with spontaneous action-potential-independent synaptic release

We superfused the voltage-gated Na^+ (Na_V) channel blocker tetrodotoxin (TTX) over the barrel cortex in awake mice to determine whether plumes were dependent on neuronal action potentials. TTX (30 μM, applied for 30 min) blocked the glutamate response to whisker stimulation in FHM2 mice, but it did not significantly decrease the frequency, diameter, duration, or amplitude of spontaneous plumes in the same animals (Figures 4A–4C, S4C, and S4D; see Figures S4A and S4B for additional control experiments).

Synchronous glutamate release is largely dependent on action potentials, although neurons also release glutamate through action-potential-independent pathways that recruit many of the same mechanisms of synaptic release (Ermolyuk et al., 2013; Kaeser and Regehr, 2014; Schneggenburger and Rosenmund, 2015). We tested the role of neural synaptic mechanisms in plume generation by inhibiting voltage-gated Ca^{2+} (Ca_V) channels with the broad channel-subtype inhibitor Ni^{2+} (1 mM) (Tottene et al., 1996; Zamponi et al., 1996), and observed a halving

Figure 3. Inefficient glutamate clearance mediates plumes

(A) Imaging schematic and AIP with plume overlay show plumes primarily occurred near the surface of the brain in putative cortical L1a. BV, blood vessel.

(B) Quantification of plume frequency by cortical layer in FHM2 (ANOVA with Bonferroni-Holm correction).

(C) Low magnification of confocal microscopical fields reveals irregular areas of reduced GLT-1a immunofluorescence (ir) within L1a (white arrowheads). Red arrowheads indicate putative GLT-1a+ glia limitans.

(D) Highly magnified electron microscopic fields of immunoperoxidase pre-embedded material exhibit a different frequency of GLT-1a+ profiles (characterized by dark electrodense products) in L1a (left) and L2/3 (right). Electron microscopy confirms GLT-1a+ profiles in the glia limitans (red arrowheads).

(E) Top: example image shows an asymmetric synapse with an adjacent GLT-1a+ astrocyte process (AsP). Arrowhead, postsynaptic density (PSD); AxT, axon terminal; Den, dendrite. Bottom: the density of GLT-1a+ AsPs was reduced in L1a compared to L2/3, resulting in a reduced total (t) density of GLT-1a+ profiles. n, neuronal.

(F) Left: asymmetric synapse without GLT-1a immunoreactivity (GLT-1a negative). Right: L1a had a larger proportion of GLT-1a negative synapses versus L2/3.

(G) For synapses containing adjacent GLT-1a+ AsPs, L1a contained a lower proportion of perisynaptic AsPs (peri.; distance was <300 nm from the edge of the active zone [AZ]/PSD) and greater proportion of extrasynaptic AsPs (extra; distance, >300 nm) compared to L2/3 ($p = 0.016$; Fisher's test). Arrowheads, edge of the AZ/PSD to the nearest AsP.

(H) TFB-TBOA was superfused though a perforated coverslip (dura intact) in awake mice to inhibit glutamate transporter function.

(I) AIP with overlay of plumes (left; 10 min) in a WT mouse before and after TFB-TBOA, as well as quantification of plume frequency across 4 WT mice (0.25–1 mM; paired-sample t test). Port, hole in coverslip.

(J) TFB-TBOA-induced plume characteristic in WT compared to spontaneous plumes in FHM2 under similar conditions (two-sample t test).

(B and J) n, number mice in parentheses. (C–I) WT. (E and F) Mann-Whitney test. Error bars represent SEM. Box and whisker show 1× and 1.5× the IQR, respectively.**$p \leq 0.01$; ***$p < 0.001$; ****$p < 0.0001$. See also Figures S2 and S3.

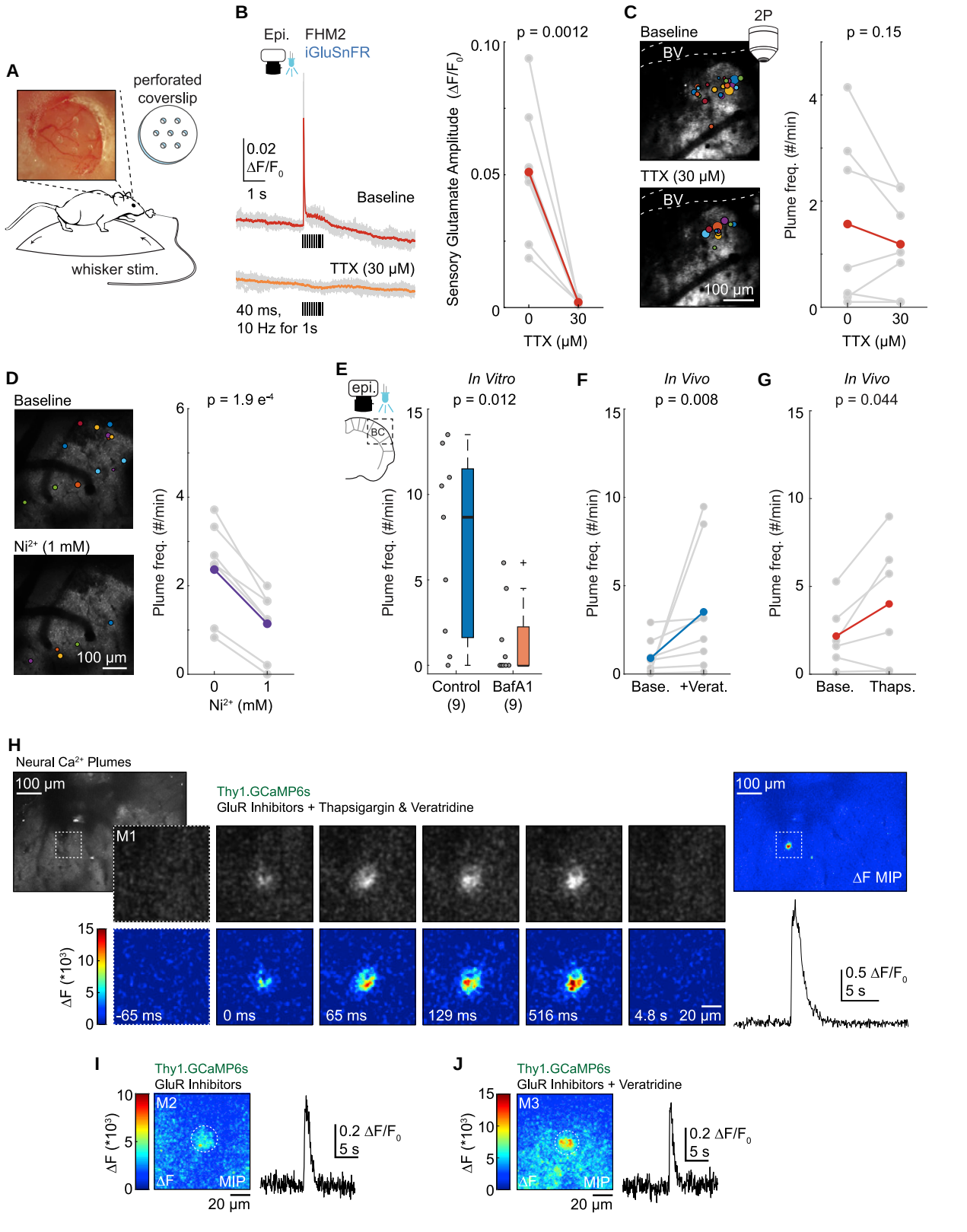

(legend on next page)

of spontaneous plume frequency compared to baseline in awake FHM2 mice (Figure 4D). However, spontaneous plumes did not depend on Ca^{2+} influx through local presynaptic NMDA receptors (Banerjee et al., 2016; Zhou et al., 2013), as DL-2-amino-5-phosphonopentanoic acid (DL-APV) did not inhibit the frequency of plumes in awake FHM2 mice (Figure S4E). These results also suggest that the inhibition of plume occurrence with Ni^{2+} was not mediated through inhibition of NMDA receptors (Marchetti and Gavazzo, 2005).

To determine whether plumes depended specifically on vesicular release, we incubated cortical slices from FHM2 mice in bafilomycin A1 (which prevents vesicular filling) and veratridine (which promotes the release of previously filled vesicles; see STAR methods; Figures S3F and S3G; Agarwal et al., 2017; Cavelier and Attwell, 2007; Fekete et al., 2009; Ulbricht, 2005; Zhou et al., 2013). Bafilomycin A1 treatment abolished plumes in over half the FHM2 slices tested and reduced the median frequency compared to both artificial cerebrospinal fluid controls (Figure S3H) and controls treated with veratridine alone (Figure 4E), consistent with vesicular release.

The Ca_V-dependent vesicular source of plume glutamate was further supported by experiments in WT cortico-hippocampal slices for which removal of extracellular Ca^{2+} significantly reduced the number of TFB-TBOA-induced plumes (Figure S3J).

Veratridine, which was used as an adjunct treatment in bafilomycin A1 experiments, was noted to significantly increase the incidence of plumes in FHM2 mice both *in vitro* (Figure S3I) and *in vivo* (Figures 4F and S4F). Veratridine increases synaptic release by inhibiting Na_V channel inactivation and increasing intracellular Ca^{2+} in neurons by both Ca_V-dependent and -independent mechanisms (Fekete et al., 2009; Ulbricht, 2005). Thus, the increase in plume incidence with veratridine provides evidence for both synaptic release and calcium dependence. Interestingly, the same concentration of veratridine (100 μM) did not induce plumes in WT mice *in vivo* (see Figure 5E below), suggesting that, like spontaneous plumes, veratridine-induced plumes depended on the impaired rate of glutamate clearance in FHM2 mice. At higher concentrations of veratridine (≥500 μM), plumes were induced in both FHM2 and WT mice (Figure 5E).

We then tested whether increasing action-potential-independent spontaneous synaptic glutamate release increased plume frequency in FHM2 mice. Sarco/endoplasmic reticulum Ca^{2+}-ATPase (SERCA) inhibitors, such as thapsigargin, increase the frequency of spontaneous miniature postsynaptic currents, at least acutely, by increasing Ca^{2+} in synaptic boutons, likely by store-operated channel opening (Emptage et al., 2001; Savić and Sciancalepore, 1998; Sharma and Vijayaraghavan, 2003). Thapsigargin increased the frequency of glutamatergic plumes in two-thirds of the FHM2 mice tested (Figure 4G). Thus, mechanistically distinct manipulations that decrease synaptic release reduced the frequency of plumes (Ni^{2+} and bafilomycin A1), whereas those that increase synaptic release increased the incidence of plumes (veratridine and thapsigargin). Despite their action potential independence, these results suggest that plumes in FHM2 mice depend on mechanisms of synaptic release.

Astrocytes are capable of Ca^{2+}-dependent vesicular glutamate release, although whether this occurs under physiological conditions *in vivo* is an area of active discussion (Fiacco and McCarthy, 2018; Savtchouk and Volterra, 2018). As the α2NKA expresses primarily in astrocytes, we tested whether the manipulation of astrocytes was capable of inducing plumes. Mechanical stimulation with a pipette and depolarizing current injections using whole-cell patch-clamp induced a Ca^{2+} response in astrocytes *in vivo* but failed to induce plumes in FHM2 mice (see Figure S5 and its legend).

Plume-like neuronal calcium transients in FHM2 mice

In FHM2 mice expressing the genetically encoded Ca^{2+} indicator GCaMP6s under the Thy1 promoter (putative excitatory projection neurons) (Chen et al., 2012; Dana et al., 2014), we observed plume-like Ca^{2+} transients that were generally circular, originated from a central location, and increased in size over time in the neuropil of L1a (Ca^{2+} plumes) (Figures S4G and S4H).

Figure 4. Glutamatergic plumes are consistent with action-potential-independent, spontaneous glutamate release from neurons

(A) Schematic illustrating compound application through a perforated coverslip.

(B) Blocking Na_V channels with TTX (30 μM) blocked the whisker-mediated glutamate response. Left: individual trials (gray) and mean (color) from a single mouse. Black bars indicate whisker stimulations (40 ms at 10 Hz for 1 s). Right: mean response amplitude (n = 7 FHM2 mice).

(C) In the same mice as (B), TTX did not inhibit the frequency of plumes (right). Left: AIP with overlay of plumes (10 min) from a single mouse.

(D) The Ca_V channel blocker Ni^{2+} (1 mM) reduced the frequency of spontaneous plumes *in vivo*, suggesting plumes depend on neuronal synaptic machinery (n = 7 FHM2 mice). Left: AIP with overlay of plumes (5 min). Images cropped for clarity.

(E) Preventing vesicular filling with bafilomycin A1 (BafA1; 4 μM) inhibited plume frequency in FHM2 cortical slices (Wilcoxon rank-sum test), confirming plumes depend on vesicular release.

(F) Inhibiting Na_V channel inactivation with a brief exposure to veratridine (+Verat.; 10 min, 100–150 μM) was sufficient to increase plume frequency *in vivo* (Wilcoxon rank-sum test; n = 8 FHM2 mice).

(G) SERCA inhibitors increase the frequency of spontaneous miniature postsynaptic currents (see Results for references), and thapsigargin (500 uM) increased the average frequency of plumes in FHM2 mice (n = 6 mice; measured during the first 10 min of application).

(H–J) Examples of neural Ca^{2+} plumes observed in the neuropil of L1a in FHM2 mice expressing GCaMP6s under the Thy1 promoter (putative excitatory neurons) with a cocktail of glutamate receptor (GluR) inhibitors (see Results and STAR methods) to isolate putative presynaptic neural Ca^{2+}.

(H) Left: AIP of L1a. Image cropped for clarity. Center: magnified panel of images depicting a neural Ca^{2+} plume over time in raw (top) and ΔF images (bottom) in the presence of GluR inhibitors and plume inducers, thapsigargin and veratridine. A Gaussian blur added to all images. Time stamps correspond to the start of the event. Images taken from the dashed square in the AIP. M1, mouse 1. Right: the MIP of the ΔF image series (top) and quantification (bottom).

(I and J) Two additional examples of neural Ca^{2+} plumes from different mice than that in (H) (M2 and M3) recorded in the presence of GluR inhibitors alone (I) or with the addition of veratridine (J). MIP of the ΔF image series (left) and quantification (right).

(B–G) Gray is animal mean, and color is grand mean. (B, C, D, and G) Paired-sample t test, one-tailed. Box and whisker show 1× and 1.5× the IQR, respectively. See also Figures S3–S5 and Video S3.

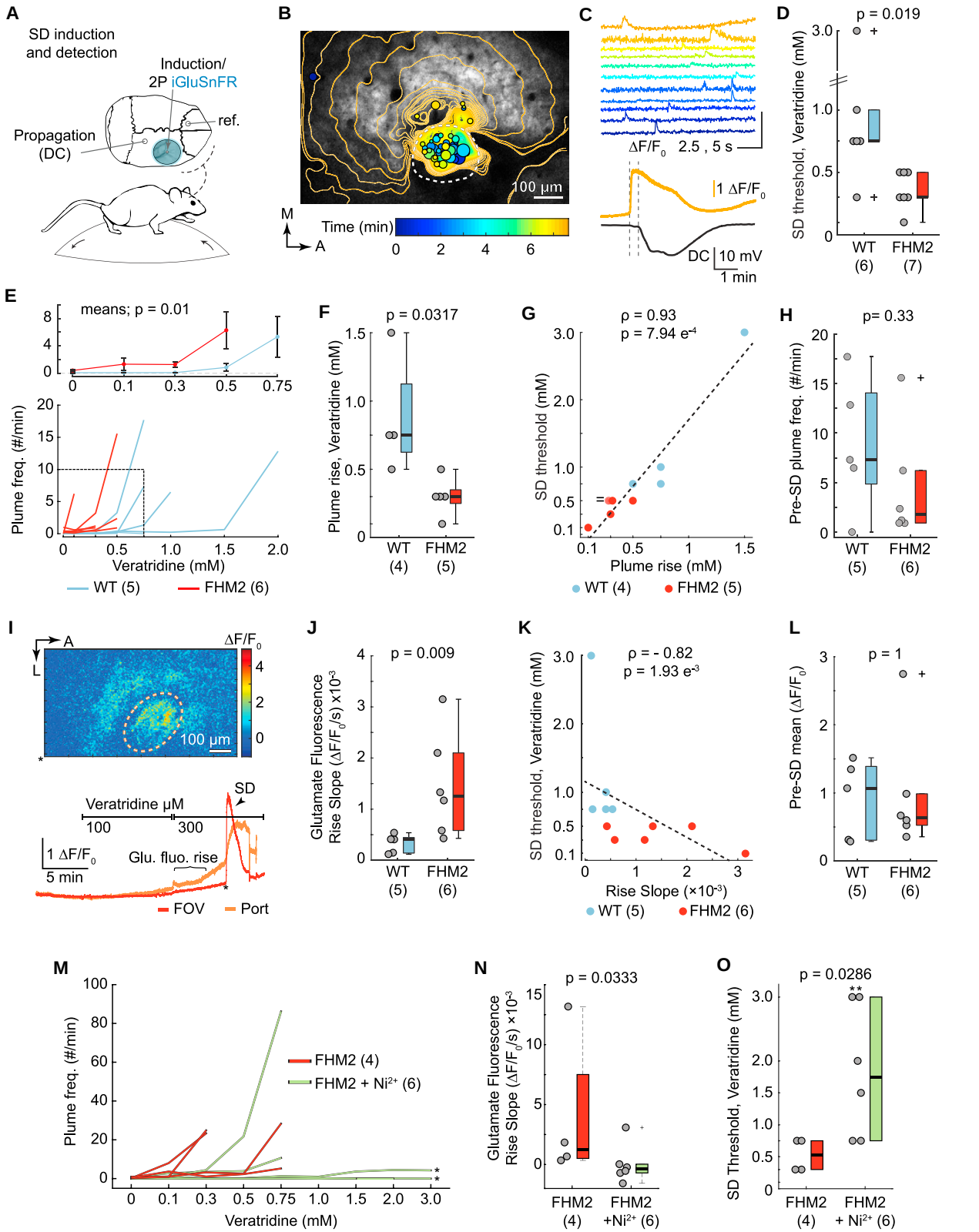

(legend on next page)

Thy1-GCaMP mouse lines express GCaMP in both presynaptic and postsynaptic neural processes. To inhibit postsynaptic Ca^{2+} due to glutamate receptor activation during plumes, we superfused a cocktail of glutamate receptor antagonists (6,7-dinitroquinoxaline-2,3-dione disodium salt [DNQX; 500 μM]; 3-((2-methyl-1,3-thiazol-4-yl)ethynyl)pyridine hydrochloride [MTEP; 500 μM]; 6-methoxy-N-(4-methoxyphenyl)-4-quinazolinamine hydrochloride [LY 456236; 200 μM]; DL-APV [1 mM]; see STAR methods). Control experiments confirmed the NMDA receptor inhibitor DL-APV inhibited Ca^{2+} activity in sparsely labeled tufted dendrites in L1 during whisker stimulation trials (Figure S4I). The cocktail of glutamate receptor antagonists reduced the median peak amplitude of the whisker-mediated Ca^{2+} response by ~56%, demonstrating successful inhibition of glutamate-receptor-mediated Ca^{2+} signaling in the neuropil of L1 (Figures S4J and S4K). The residual Ca^{2+} response was presumably comprised of mostly presynaptic neural signaling. In the same mice, we observed neural Ca^{2+} plumes in L1a with glutamate receptor inhibitors alone, or with receptor inhibitors plus plume inducers (veratridine and thapsigargin) (Figures 4H–4J; Video S3). Thus, our results suggest that Ca^{2+} plumes do not require glutamate receptors and that at least a portion of the Ca^{2+} increase during Ca^{2+} plumes is presynaptic. These findings are consistent with the hypothesis that plumes are due to Ca^{2+}-dependent neuronal vesicular glutamate release.

Increased plume frequency precedes the onset of veratridine-induced SD

Impaired glutamate clearance can account for the increased susceptibility to SD in FHM2 mice (Capuani et al., 2016), as well as the increased incidence of plumes in these animals (Figures 3, S2, and S3). This prompted an examination of the possible relevance of glutamatergic plumes to SD onset. We implanted a coverslip containing a single perforation over the barrel cortex (~200- to 300-μm diameter, near the minimum size needed to induce SD with KCl in brain slices) (Tang et al., 2014) and recorded inside the perforation with 2-photon microscopy during application of SD-inducing stimuli in WT and FHM2 mice (Figures 5A and 5B). To our knowledge, these are the first 2-photon recordings of SD induction at cellular resolution in awake animals.

Veratridine can initiate SD *in vitro* and *in vivo* (Ashton et al., 1990; Krivánek, 1978), thus providing an opportunity to investigate plumes and their relationship to SD. Under increasing concentrations of veratridine (higher than those used to investigate mechanisms of glutamate release in plumes; Figure 4), both plume frequency and basal glutamate fluorescence increased within the induction port. The area in which plume and basal glutamate fluorescence increased then became the origin point of SD (Figures 5B and 5I; Video S4). SD itself caused a steep rise in glutamate fluorescence that propagated into surrounding tissue, which was confirmed by electrode recordings showing the negative shift in direct current field potential that characterizes the phenomenon (Enger et al., 2015; Figures 5B and 5C).

The average concentration of veratridine necessary to induce SD was lower in FHM2 mice than in WT mice (Figure 5D), which is consistent with previous findings of decreased SD threshold using electrical stimulation and KCl in FHM2 mice (Capuani et al., 2016; Leo et al., 2011). Similarly, the rise in plume frequency started at lower concentrations of veratridine in FHM2 versus WT (Figures 5E and 5F) and was positively correlated with SD

Figure 5. A rise in plume frequency predicts onset of veratridine-induced SD regardless of genotype

(A) Glutamate fluorescence was recorded during SD induction by superfusing veratridine through a single perforation in the coverslip. Direct current (DC) confirmed SD propagation.

(B) Veratridine induced plumes and a rise in basal glutamate fluorescence prior to SD induction. Temporal contour lines and plume overlays (colored circles) illustrate the glutamate wavefront and location (as well as size) of plumes prior to and with SD initiation, respectively. The color of the contour lines and the plume overlays correspond with time. Dashed circle, hole in the coverslip.

(C) Corresponds with (B). Top: traces of selected plumes leading up to SD. Bottom: SD was measured as a propagating rise in glutamate fluorescence (proximal to induction site) and DC shift (distal). Vertical dotted lines denote the start of SD in both recordings, illustrating propagation of the wave across the cortex. Glutamate quantification over entire field of view (FOV; 918 × 569 μm).

(D) The concentration of veratridine that induced SD (threshold) was lower in FHM2 than in WT.

(E) Plume frequency rose with increasing concentrations of veratridine leading up to SD onset in individual mice (bottom) and genotype averages (top; repeated-measures two-way ANOVA).

(F and G) The rise in plume frequency occurred at lower concentrations of veratridine in FHM2 than in WT (F) and correlated with SD threshold across individual animals (G). (G) contains two overlapping points (0.3 mM plume rise, 0.5 mM SD threshold; " = " in figure).

(H) The frequency of plumes prior to SD (at relative concentrations of veratridine for individual mice) was similar between the two genotypes.

(I) Basal glutamate fluorescence increased inside the induction port prior to SD. Top: example $\Delta F/F_0$ image. Bottom: corresponding fluorescence traces; *, time of $\Delta F/F_0$ image.

(J and K) The slope of the rise in basal glutamate fluorescence was steeper in FHM2 than in WT mice (J) and correlated with SD threshold across individual animals (K). Slope was measured up to the SD threshold for individual animals or 750 μM veratridine—the median threshold for WT—for comparison.

(L) The level of basal glutamate fluorescence (mean $\Delta F/F_0$) at the concentration of veratridine that induced SD in individual mice was comparable in both genotypes.

(M–O) Ni^{2+} (10 mM) inhibited the rise in plume frequency and basal glutamate fluorescence, as well as increased the SD threshold in FHM2 mice.

(M) Similar to (E), quantification of the plume frequency with increasing concentrations of veratridine leading up to SD onset in individual mice. Ni^{2+} blocked or inhibited the rise in plume frequency in 4 out of 6 FHM2 mice. *, no SD.

(N) Ni^{2+} inhibited the rise in basal glutamate fluorescence with veratridine, quantified as a decrease in the average slope.

(O) Ni^{2+} increased the concentration of veratridine needed to induce SD (threshold) in FHM2 mice. *, no SD.

n, number of mice in parentheses. (D, F, H, J, L, N, and O) Wilcoxon rank-sum test (N and O used a one-tailed version). (G and K) Spearman's Rho. Two mice were excluded from (F) and (G) (1 from each genotype) because a rise in plume frequency did not occur. These mice were included in (H)–(L). Box and whisker show 1× and 1.5× the IQR, respectively. See also Figure S6 and Video S4.

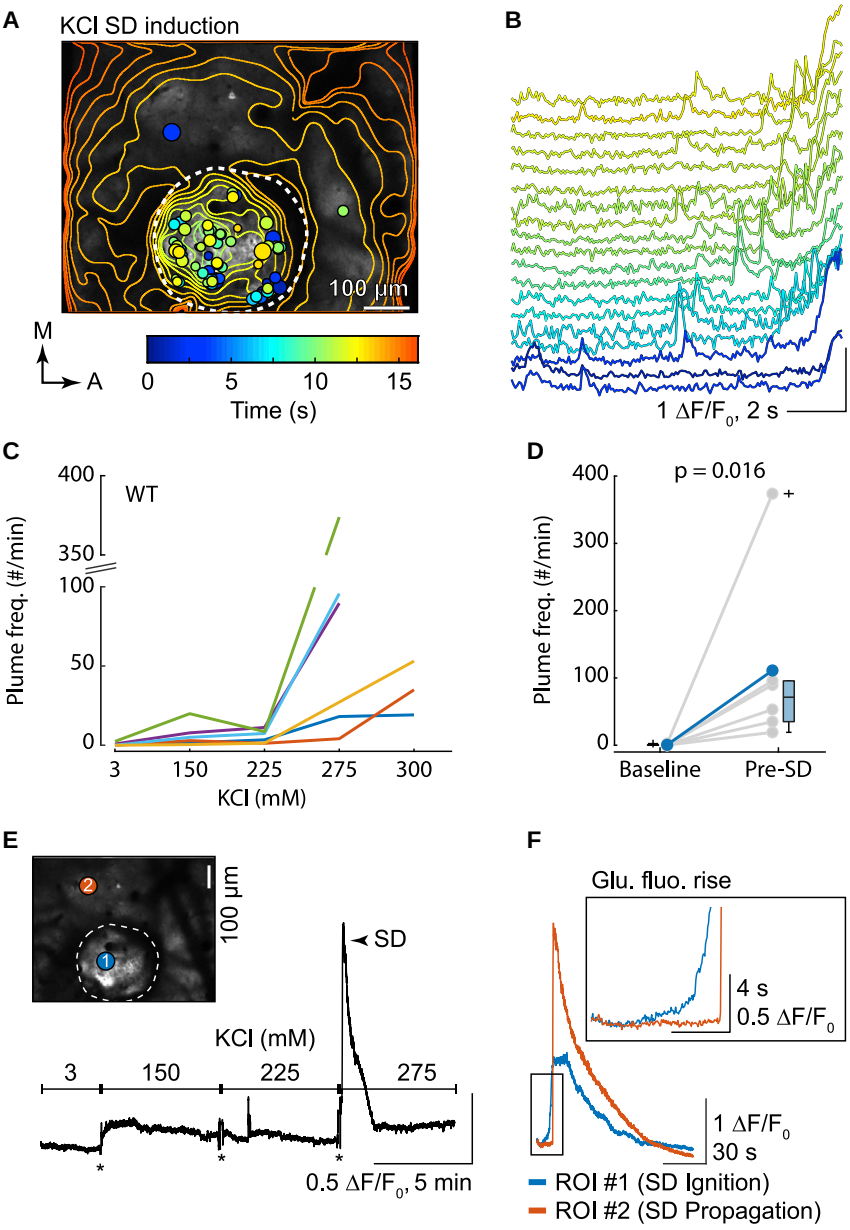

Figure 6. A rise in plume frequency precedes the onset of KCl-induced SD in WT mice

(A) KCl induced plumes prior to SD induction in a single WT mouse. Like Figure 5B, plume overlays and temporal contour lines illustrate the location and size of plumes, as well as the glutamate wavefront, respectively.

(B) Select traces of plumes from the same animal as in (A). Color corresponds with the colorbar in (A). Multiple plumes are present in some traces, indicating multiple events occurred in the same location. The increase in basal fluorescence over time is due to the rise in glutamate fluorescence ahead of SD initiation (see E and F below).

(C) The frequency of plumes with increasing KCl concentrations up to SD induction for individual animals (n = 6 WT mice).

(D) Quantification of the plume frequency during baseline (KCl = 3 mM) and the concentration of KCl that induced SD (relative for each animal) (Wilcoxon signed-rank test; n = 6 WT mice). Gray is animal mean, and color is grand mean. Box and whisker show 1× and 1.5× the IQR, respectively.

(E) Basal glutamate fluorescence was relatively stable prior to SD induction, despite increasing concentrations of KCl. An example trace (black) from the same animal as in (A) and (B). *, imaging artifact due to the exchange of fluids in the imaging well (truncated for illustration).

(F) Basal glutamate fluorescence increased as a brief ramp (Glu. fluo. rise) at the SD induction site just prior to SD initiation (region of interest [ROI] #1, blue trace; corresponds with the colored circle in the inset image of E). By contrast, SD propagation induced a sharp rise in glutamate fluorescence, but no ramp (ROI #2, orange trace). Traces start from the application of 275 mM KCl. A representative of n = 6 WT mice (see Results).

onset in individual mice regardless of genotype (Figures 5G and S6B). Of note, 1 mouse from each genotype did not have an increase in plume frequency prior to SD, suggesting a rise in plume occurrence typically correlates with SD onset, but may not necessarily be required, at least for veratridine-induced SD (see Figures S6B–S6E for additional correlations with veratridine and Figure 6 for examples of SD initiation with KCl). Interestingly, the plume frequency just prior to SD onset was similar in WT and FHM2 mice, despite the fact that the concentration of veratridine that induced SD was lower in FHM2 mice (Figures 5H and S6C). These results establish that plumes are not only a phenotype of the FHM2 mutation but also a previously unknown form of glutamate dysregulation that manifests as the network approaches SD.

The slope of the rise in basal glutamate fluorescence was steeper in FHM2 than in WT mice (Figure 5J) and was negatively correlated with SD threshold, with a steeper slope correlating with a lower threshold (Figures 5K and S6D). Although the concentration of veratridine was lower in FHM2 at any given level of basal glutamate fluorescence, mean basal fluorescence just prior to SD onset was similar in both genotypes (Figures 5L and S6E). These results are consistent with a threshold level of glutamate associated with SD onset regardless of genotype and suggest that differences in SD susceptibility, at least in FHM2, relate to the rate at which the glutamate threshold is achieved, rather than a difference in the glutamate threshold itself.

To examine the possibility of a causal role for plumes and glutamate in SD initiation, we asked whether inhibiting Ca_V channels and glutamate release with Ni^{2+} would inhibit veratridine-induced SD. In control FHM2 mice (treated with veratridine but not Ni^{2+}), we again observed a rise in plume frequency and basal glutamate fluorescence before SD onset (Figures 5M and 5N). Ni^{2+} (10 mM) inhibited the incidence of plumes in most mice

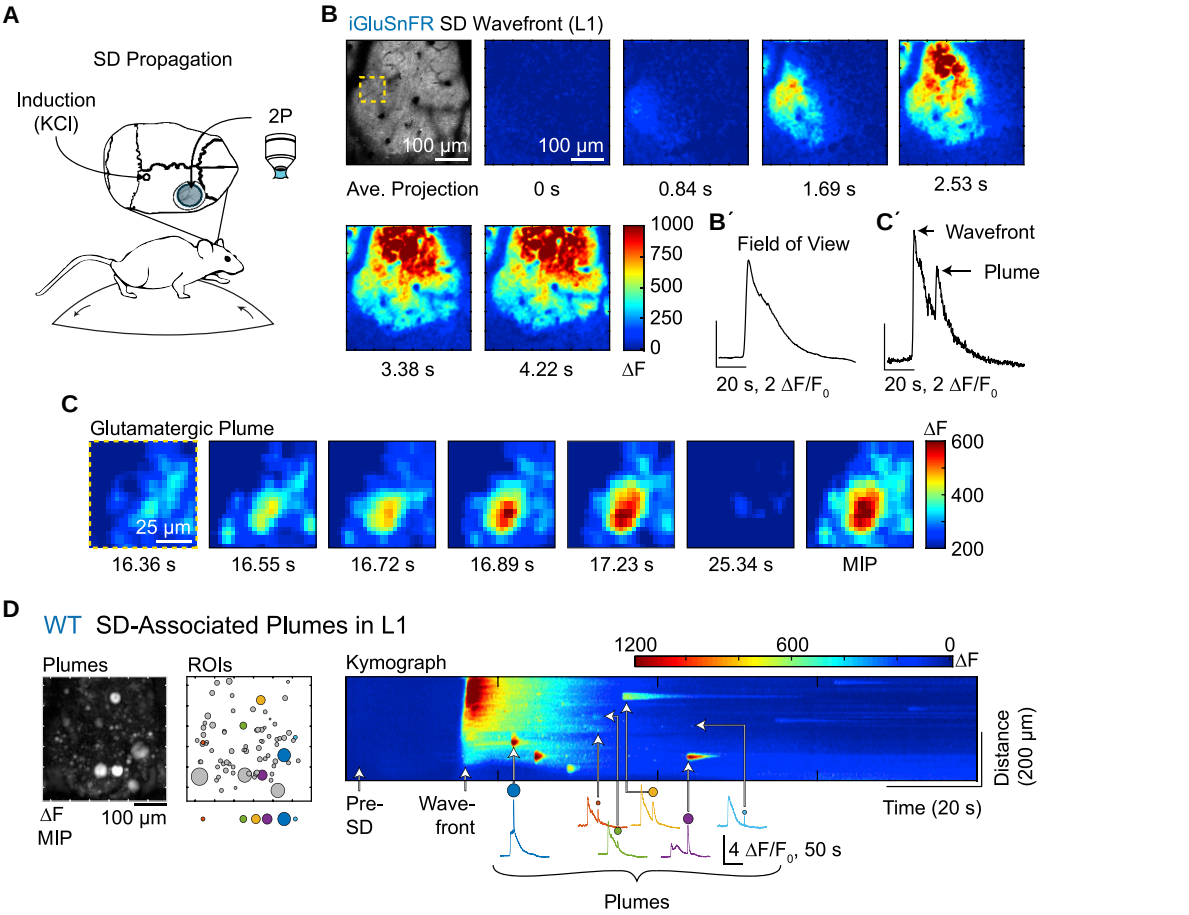

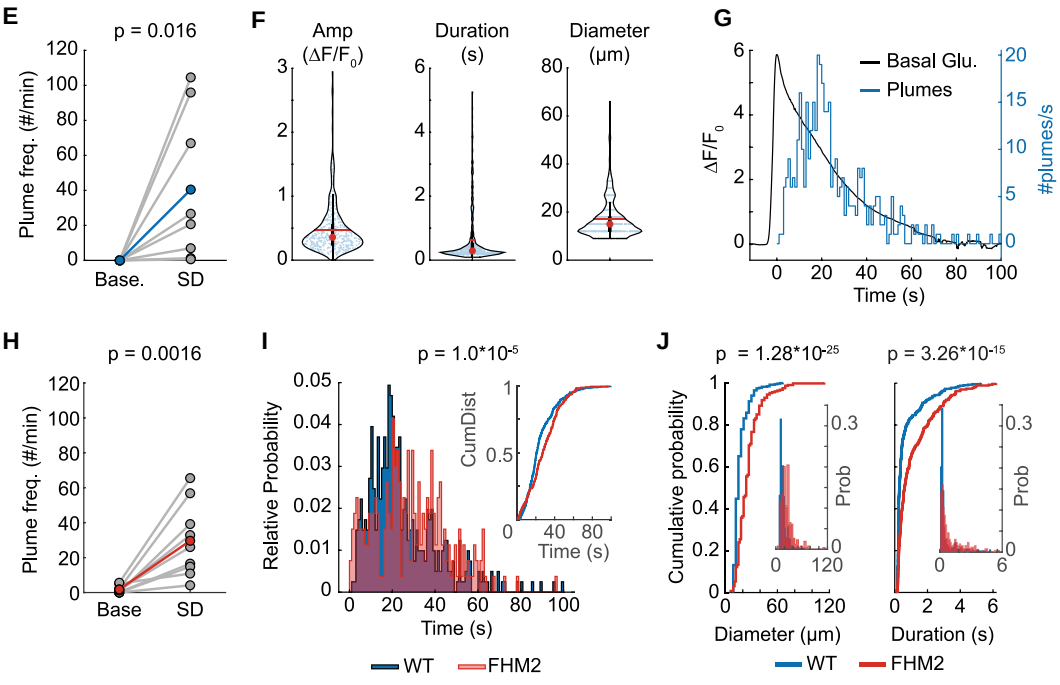

(legend on next page)

(Figure 5M), eliminated the rise in basal glutamate fluorescence (Figure 5N), and increased the median SD threshold by more than 3-fold relative to controls (Figure 5O). Ni^{2+} prevented SD induction in 4 out of 6 FHM2 mice using concentrations of veratridine that induced SD in all control FHM2 mice ($\leq$750 μM) and in 2 out of 6 FHM2 mice by using higher concentrations of veratridine ($\leq$3 mM) (Figures 5D and 5O). These findings are consistent with a critical role of Ca_V-dependent glutamate release in veratridine-induced SD in FHM2 mice and suggest that additional glutamate-independent mechanisms may contribute to SD ignition at higher concentrations of veratridine ($\geq$750 μM).

Overall, we observed 2 novel forms of glutamate dysregulation—glutamatergic plumes and an increase in basal glutamate fluorescence—at the ignition site of veratridine-induced SD. Both plumes and the increase in basal fluorescence were elicited at lower veratridine concentrations in FHM2 mice, but they correlated with SD threshold in both genotypes. Inhibiting the rise in plume frequency and basal glutamate fluorescence with Ni^{2+} inhibited SD in FHM2 mice, suggesting plumes and extracellular glutamate may play a causal role in establishing the threshold for veratridine-induced SD.

Increased plume frequency precedes the onset of K^+-induced SD

To determine whether the presence of glutamatergic plumes was generalizable in SD induction, we used increasing concentrations of KCl delivered through a single hole in the coverslip in WT mice (Figure 6A). K^+ thresholding is arguably the most common experimental model of SD induction, and elevated extracellular K^+ is likely a vital component of the initial depolarization needed to generate SD in otherwise healthy tissue (Pietrobon and Moskowitz, 2014; Somjen, 2001). Similar to treatment with veratridine, all mice showed an increase in plume frequency within and adjacent to the induction port preceding KCl-induced SD. The steepest rise in plume frequency occurred just prior to SD onset in 5 out of 6 mice (Figures 6C and 6D).

In contrast to veratridine treatment, basal glutamate fluorescence increased at the initiation site only 6.56 ± 3.35 s (mean ± standard deviation; n = 6 WT mice) before SD onset (Figures 6B and 6F; compare with Figure 5I) and did not rise with increasing concentrations of KCl (Figure 6E).

These results confirm the association of plumes with SD initiation by using a more generalizable induction technique, with KCl inducing a rise in plume frequency and basal glutamate fluorescence that preceded SD onset in WT mice.

Glutamatergic plumes follow but do not lead the propagating wavefront of SD

Once initiated, SD propagates across the cortex (Pietrobon and Moskowitz, 2014; Somjen, 2001). To determine whether plumes preceded the propagating SD wavefront, we superfused KCl (1 M) through a small burr hole near lambda to induce an SD that propagated several mm into the imaging window over the barrel cortex (intact coverslip) (Figure 7A). In contrast to SD initiation, a rise in plume frequency and basal glutamate fluorescence did not precede the propagating SD wavefront in WT or FHM2 mice in L1 or L2/3 (Figures 7B, 7D, and S7). Instead, we observed a large increase in basal glutamate at (but not before) the wavefront and a rise in plume frequency only after the wavefront during the depolarization phase of SD (Figures 7B–7E, 7H, and S7).

We consistently observed a temporal lag in the occurrence of plumes relative to the wavefront in L1 (including both L1a and L1b). A histogram aligning plume timing to the peak of basal SD glutamate fluorescence showed that the plume number reached its peak 18.5 s after peak fluorescence in WT mice

Figure 7. Continued glutamate release in the form of glutamatergic plumes following the propagating SD wavefront

(A) KCl (1 M) superfused through a small burr hole near lambda induced an SD that propagated into the imaging window, placed over the barrel cortex (using an intact coverslip).

(B) ΔF images quantify the increase in glutamate fluorescence with the propagating SD wave in L1 of a WT mouse. Note that glutamatergic plumes do not precede the SD glutamate wavefront. Each time stamp is relative to the first image (0 s). Top left: AIP prior to SD (raw image). The yellow dashed box corresponds to the magnified images in (C). See (B') for quantification.

(C) A glutamatergic plume that occurred during SD depolarization (following the wavefront) in the same animal as in (B). Time stamp corresponds to 0 s in (B). Peak fluorescence of the plume occurred at 17.23 s. For illustrative purposes, the lower range of ΔF was increased from 0 to 200 ΔF to control for increased basal fluorescence during SD. See (C') for quantification.

(D) An example of all SD-induced plumes in L1 (same mouse as in B). Left: a MIP provides a spatial map of all plumes that occurred during SD depolarization. Center: plume ROIs (circles), with a select set (colored circles) highlighted below and quantified to the right. Right: a ΔF kymograph from the entire FOV illustrates the SD wavefront and all SD-associated plumes over time. Note that plumes occurred after the SD wavefront (representative of n = 8 WT and 9 FHM2 mice). For traces of plumes (bottom), the initial rise in fluorescence is the glutamate SD wavefront, and the colored ROI sits directly above the plume.

(E) The frequency of plumes during SD depolarization in L1 was significantly higher than in baseline recordings (prior to SD induction) in WT mice (n = 8 mice).

(F) Characteristics of SD-induced plumes from WT mice in cortical L1. Red circle, median; red horizontal line, mean. Box and whisker show 1× and 1.5× the IQR, respectively.

(G) A histogram (blue) shows the number of plumes/s over time from all WT mice in L1 and illustrates the latency of each plume relative to the peak (0 s) in basal glutamate fluorescence (Basal Glu.; black). The peak of the plume frequency occurred at 18.5 s. Bin width, 1 s.

(H) Similar to WT, SD depolarization increased the frequency of plumes in L1 in FHM2 mice compared to baseline recordings (prior to SD induction; n = 9 mice).

(I) A histogram of the number of plumes/s over time in FHM2 mice (red) overlaid with WT (blue; same events as in G), shows that plumes persisted for a longer period following the SD wavefront (time = 0 s) in FHM2 mice. Both histograms were normalized to their relative probability. The peak of the plume frequency in FHM2 mice occurred at 20.5 s (see STAR methods). Inset: the cumulative distribution of plumes over time for both genotypes.

(J) SD-induced plumes were larger in diameter (left) and had a longer duration (right) in FHM2 mice than in WT. Plots show a cumulative probability (traces), and insets are a histogram of relative probability (prob.). Both histograms use the same x axis as their respective cumulative plots.

(E and H) Paired-sample t test, one-tailed. (F and G) n = 405 plumes from 8 WT mice. (I and J) Two-sample Kolmogorov-Smirnov test; n = 264 plumes from 9 FHM2 mice. (B–G) WT. (H) FHM2.

See also Figure S7.

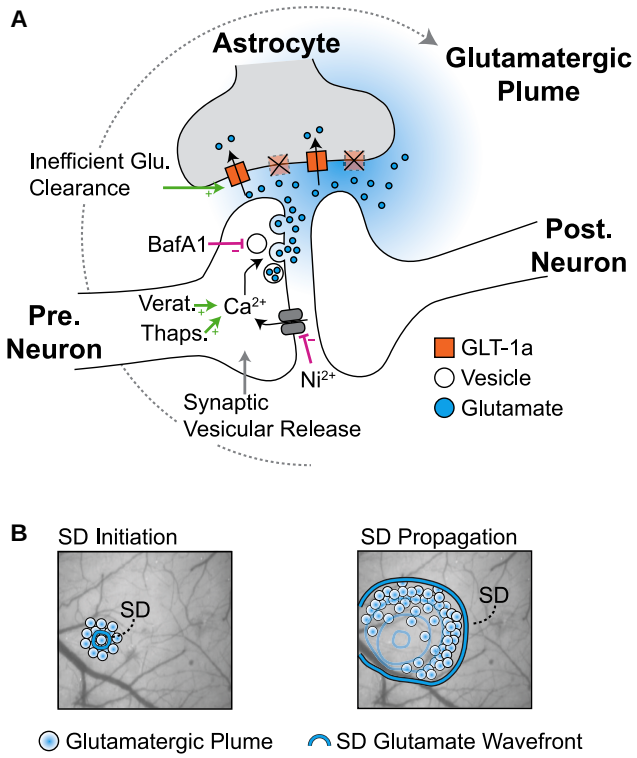

Figure 8. A model of glutamatergic plumes

(A) Glutamate release during plumes is likely due to Ca^{2+}-mediated vesicular release from neurons, as compounds that inhibit release (Ni^{2+} and BafA1) reduce the frequency of plumes (pink lines), whereas those that promote release (veratridine and thapsigargin) increase the frequency of plumes (green arrows). Once glutamate is released, the presence of plumes is gated by impaired or inefficient glutamate clearance by astrocytes. Stimuli that depolarize neural membranes (KCl and SD) are sufficient to induce plumes. This model illustrates glutamate release from a single synapse for clarity, although release from multiple synapses may contribute to a single plume (see Discussion). Pre., presynaptic; Post., postsynaptic.

(B) The relationship of plumes to SD. Left: an increase in plume frequency precedes veratridine-induced SD in FHM2 and WT mice, as well as KCl-induced SD in WT, at the initiation site. Right: as SD propagates into the surrounding cortex, plumes occur during the depolarization phase, following the wavefront. Additional work is needed to determine whether the mechanisms of plume generation during SD depolarization overlap with those during spontaneous plumes and SD initiation.

(Figure 7G). In both genotypes, the occurrence of plumes resolved with the decay in basal glutamate fluorescence (Figure 7G), suggesting plumes subsided as clearance mechanisms were able to buffer extracellular glutamate back to pre-SD levels. The frequency of SD-induced plumes was similar between WT and FHM2 mice (Figure S7B), although plumes persisted for a longer period following the wavefront in FHM2 mice versus WT, reaching a peak at 20.5 s in FHM2 (Figure 7I). SD-induced plumes were larger in diameter and had a longer duration in FHM2 mice than in the WT (Figure 7J), suggesting astrocyte clearance efficiency may also mediate the temporal and spatial characteristics of plumes during SD depolarization.

Contrary to L1, very few plumes occurred in L2/3 during SD depolarization in both genotypes (Figure S7), suggesting that similar to spontaneous plumes, SD-induced plumes may also depend on laminar architecture.

In summary, we find that glutamatergic plumes do not precede, and instead follow, the propagating wavefront of SD and may constitute a second phase of glutamate release following the initial wavefront in L1.

DISCUSSION

The availability of fluorescent glutamate imaging has allowed us to investigate the significance of glutamate signaling as a disease mechanism in awake animals. We found that the FHM2 mutation was associated with several forms of glutamate dysregulation compared to WT littermates: slower clearance rate during sensory processing (Figure 1), spontaneous glutamatergic plumes under basal conditions (Figure 2), and a rise in plume frequency and accelerated extracellular glutamate accumulation as the network approached the SD threshold (Figure 5).

Glutamatergic plumes appear to be previously uncharacterized glutamate signaling events arising as a consequence of impaired astrocyte clearance of synaptically released glutamate (Figure 8A). Three findings support the key role of impaired glutamate clearance by astrocytes for plume generation: (1) spontaneous plumes occur in FHM2 mice that have a reduced rate of clearance of synaptically released glutamate and reduced density of GLT-1a glutamate transporters in perisynaptic astrocytic processes (Capuani et al., 2016) and are almost completely absent in WT mice (Figure 2); (2) the spontaneous plumes in FHM2 are predominantly located in L1a, where astrocyte somas are almost absent (Figure S2; McCaslin et al., 2011), and in comparison with L2/3, the density of GLT-1a+ astrocyte processes is reduced and the percentage of excitatory synapses lacking GLT-1a+ perisynaptic astrocytes processes is increased (Figures 3 and S2); and (3) plumes occur in WT mice after pharmacological inhibition of glutamate transporters (Figures 3H–3J).

Although the incidence of plumes is closely related to impaired astrocyte uptake, the glutamate release during plumes mirrors mechanisms of spontaneous synaptic release. First, although plume occurrence is action-potential-independent, it is strongly reduced by inhibition of vesicular filling and broad Ca_V channel antagonism (Figures 4, 5, and S3). Second, compounds that increase the frequency of synaptic release (veratridine, K^+, and thapsigargin) also increased the frequency of plumes (Figures 4, 5, 6, and S4). Third, we observed neural Ca^{2+} transients in the neuropil of L1a that mimicked the morphology and spatial spread of glutamatergic plumes and persisted after glutamate receptor inhibition (Figures 4H–4J). The inhibition of plumes with Ni^{2+}, but not TTX, suggests that action-potential-independent opening of Ca_V channels at L1a presynaptic terminals may underlie the spontaneous synaptic glutamate release during plumes. The relatively depolarized resting potential of neurons in awake animals (Constantinople and Bruno, 2011) and consequent increased open probability of Ca_V channels (Awatramani et al., 2005) might result in the stochastic opening of a sufficient number of presynaptic Ca_V channels to trigger glutamate release and give rise to a plume in L1a, given the reduced glutamate clearance capacity in this layer (Figures 3 and S2). The higher

probability of plumes during upstates than during downstates in anesthetized animals supports this hypothesis (Figure S5). However, the size and spread of neural Ca^{2+} plumes suggests the recruitment of multiple axons, at least during larger diameter events (~20 μm) (Figures 4H–4J) and opens the possibility of other factors influencing glutamate release during plumes. The impairment of K^+ clearance in FHM2 mice (Capuani et al., 2016) brings up the intriguing question of whether elevations in extracellular K^+ could provide a local depolarizing stimulus to several synaptic terminals and obviate the need for action potentials in glutamate release during plumes. Indeed, high concentrations of KCl were sufficient to induce a high frequency of plumes in WT mice (Figure 6).

Of broader relevance to neurological disease, the induction of plumes in WT mice under conditions causing larger impairments of glutamate clearance or ionic homeostasis than the FHM2 mutation (Figures 3, 5, and 6) shows that plumes do not necessarily require α2NKA dysfunction. Moreover, we find that a rise in plume frequency (along with basal glutamate fluorescence) precedes SD onset with 2 different induction methods—veratridine in both FHM2 and WT (Figure 5) and KCl in WT (Figure 6). These results establish plumes as a previously unknown form of glutamate dysregulation that manifests as the network approaches SD, linking plumes to the key translational phenotype of FHM2 and all other models of migraine with aura. Interestingly, in veratridine experiments in which we examined both FHM2 and WT animals, a similar threshold level of plume frequency and basal glutamate fluorescence was associated with SD onset in both genotypes (Figures 5H, 5L, S6C, and S6E). However, the concentration of veratridine producing the threshold levels was lower in FHM2 than in WT mice, consistent with previous findings of decreased SD threshold using electrical or KCl stimulation in FHM2 mice (Capuani et al., 2016; Leo et al., 2011).

The impaired rate of glutamate clearance in FHM2, as well as the enhanced $Ca_V2.1$-dependent glutamate release in FHM1 (a genetic migraine mutation causing gain of function of $Ca_V2.1$ channels) (Pietrobon, 2013), can largely account for the decreased SD threshold in cortical slices (Capuani et al., 2016; Tottene et al., 2009). These findings led us to propose a model in which the depolarizing stimulus releases enough glutamate to overwhelm the binding capacity of astrocytic glutamate transporters, thus leading to cooperative activation of synaptic and extrasynaptic NMDA receptors in a number sufficient to initiate the positive feedback cycle that ignites SD (Pietrobon and Brennan, 2019; Pietrobon and Moskowitz, 2014).

The present study provides the first direct support of a threshold level of extracellular glutamate for SD ignition, regardless of genotype. The prediction of the model is that increased susceptibility to SD in both FHM1 and FHM2 (Capuani et al., 2016; Tottene et al., 2009) is due to the fact that the glutamate threshold is reached with stimuli of lower intensity. Given that impaired glutamate clearance primarily affects the activation of NMDA receptors (Arnth-Jensen et al., 2002; Tsukada et al., 2005) and FHM2 mice have facilitated NMDA spikes in the tufted dendrites of pyramidal neurons in L1 (Romanos et al., 2020), our additional finding of a threshold level of plumes for SD ignition, regardless of genotype, suggests a possible role of plumes in the cooperative activation of NMDA receptors necessary for SD ignition. In addition, the inhibition of plumes and SD with Ni^{2+} appears to underscore the broader role of Ca_V channels in SD susceptibility and migraine pathophysiology outside of FHM1 (Eikermann-Haerter et al., 2015; van den Maagdenberg et al., 2004; Pietrobon, 2013; Tottene et al., 2009, 2011). Similar mechanisms might explain the susceptibility to SD in the CK1δ model of non-hemiplegic migraine (Brennan et al., 2013), which shows a putative presynaptic Ca^{2+}-dependent decrease in the adaptation of excitatory synapses (Suryavanshi et al., 2019).

Although we find that plumes and basal glutamate fluorescence precede SD onset at its origin site, we observe an inverse temporal phenotype during SD propagation, with the SD depolarization wavefront preceding a barrage of plumes in both WT and FHM2 mice in L1 (Figures 7, S7, and 8B). Though depression of spontaneous and evoked cortical electrical activity is a hallmark of SD in both animal models and humans (Dreier et al., 2017; Leao, 1944; Pietrobon and Moskowitz, 2014; Somjen, 2001), the presence of plumes demonstrates continued glutamate release during SD depolarization in an awake animal. These findings agree with single neuron recordings showing continued synaptic activity during SD that is largely independent of action potentials (Aiba and Shuttleworth, 2012). Indeed, SD-induced plumes reach their peak occurrence (Figure 7G) at a time when spontaneous and evoked action potentials are not observed (Aiba and Shuttleworth, 2012; Lindquist and Shuttleworth, 2012; Sawant-Pokam et al., 2017), suggesting that similar to spontaneous plumes (Figures 4B and 4C), SD-induced plumes do not require action potentials. Although the mechanism of spontaneous plumes in FHM2 likely informs the mechanism of SD-induced plumes (e.g., similar laminarity), we cannot exclude that plumes during SD originate, at least in part, from other cellular sources or mechanisms of release (Basarsky et al., 1999; Rossi et al., 2000; Wu et al., 2018; Zhou et al., 2013).

Combined with our findings that inefficient glutamate clearance gates spontaneous plumes in FHM2 mice (Figures 3, S2, and S3), the presence of plumes suggests impaired handling of glutamate release during the SD depolarization (Figures 7 and S7). Indeed, the large K^+ and Na^+ ion gradient changes (Pietrobon and Moskowitz, 2014), and the depolarization itself, are expected to decrease the cycling rate of glutamate transporters (Danbolt, 2001; Vandenberg and Ryan, 2013). Impaired handling of glutamate release—now including plumes—during SD depolarization may be of particular importance to stroke or other injuries in which SDs occur, as inhibiting glutamate transporters prolongs the duration of the direct current shift during SD and induces cortical lesions in otherwise healthy tissue (Hinzman et al., 2015).

Many questions remain about plumes, including their precise relationship with synaptic release, as well as the breadth of their incidence in other neurological disease models. We have shown that glutamatergic plumes are non-canonical, calcium-dependent glutamate signaling events, driven by both astrocytic glutamate clearance impairment and neuronal action-potential-independent release that occur spontaneously in the FHM2 model of migraine with aura. The association of plumes with SD and with experimental conditions germane to neuronal injury suggests plumes may represent a broadly relevant mechanism of neurological disease.

STAR★METHODS

Detailed methods are provided in the online version of this paper and include the following:

- KEY RESOURCES TABLE
- RESOURCE AVAILABILITY
  - Lead contact
  - Materials availability
  - Data and code availability
- EXPERIMENTAL MODEL AND SUBJECT DETAILS
- METHOD DETAILS
  - Experimental design
  - Viral injections
  - Surgery for awake imaging
  - Perforated coverslips
  - *In vivo* awake recording trials
  - *In vivo* optical recording
  - *In vivo* electrophysiology
  - *In vivo* pharmacology
  - *In vivo* recording of SD initiation
  - *In vivo* recording of SD propagation
  - Brain slice preparation
  - *In vitro* optical recording
  - *In vitro* electrophysiology
  - *In vitro* pharmacology
  - GLT-1a Immunofluorescence
  - Confocal microscopy
  - Pre-embedding electron microscopy
  - Immunoperoxidase and pre-embedding procedure
- QUANTIFICATION AND STATISTICAL ANALYSIS
  - Glutamatergic plumes
  - Sensory glutamate
  - Recording during SD initiation
  - Recording during SD propagation
  - *In vivo* laminar designation
  - EM data collection and analysis
  - Statistics

SUPPLEMENTAL INFORMATION

Supplemental Information can be found online at https://doi.org/10.1016/j.neuron.2020.11.018.

ACKNOWLEDGMENTS

We thank Giorgio Casari for the FHM2 mice, Nicholas McKean for help with viral injections, Mirko Santello for discussion of results, and Loren L. Looger and the Howard Hughes Medical Institute for providing iGluSnFR to the research community. This work was supported by the National Institutes of Health, United States R01 NS085413 and NS102978 (K.C.B.), F31 NS105531 (P.D.P.), R01 NS106901 and P20 GM109089 (C.W.S.), and T32 HL007736 (K.M.R.); the National Science Foundation, United States GRFP (P.D.P.); and the Telethon Foundation, Italy TI-GGP14234 (D.P.), PRIN 2017ANP5L8 (D.P.), PRIN 2010JFYFY2_006 (F.C. and D.P.), PRIN 2015H4K2CR (F.C.), and PSA PJ040046_2018 (F.C.).

AUTHOR CONTRIBUTIONS

P.D.P., D.P., and K.C.B. designed the study and wrote the manuscript. P.D.P., P.S., K.M.R., P.A.S.-P., M.M., and A.P. performed experiments and analyzed data. D.K. and J.J.T. provided technical direction. K.C.B., D.P., F.C., and C.W.S. provided supervision. All authors contributed writing and approved the manuscript.

DECLARATION OF INTERESTS

The authors declare no competing interests.

Received: December 30, 2019
Revised: October 9, 2020
Accepted: November 17, 2020
Published: December 14, 2020

SUPPORTING CITATIONS

The following references appear in the supplemental information: Amzica, 2002, Angulo et al., 2004, Araque et al., 1998a, Araque et al., 1998b, Araque et al., 2000, Chen et al., 2013, Fellin et al., 2004, Gómez-Gonzalo et al., 2018, Innocenti et al., 2000, Kang et al., 1998, Mishima and Hirase, 2010, Ni and Parpura, 2009, Perea and Araque, 2005, Perea et al., 2014, Poskanzer and Yuste, 2016, Sasaki et al., 2012.

REFERENCES

Agarwal, A., Wu, P.-H., Hughes, E.G., Fukaya, M., Tischfield, M.A., Langseth, A.J., Wirtz, D., and Bergles, D.E. (2017). Transient opening of the mitochondrial permeability transition pore induces microdomain calcium transients in astrocyte processes. Neuron *93*, 587–605.e7.

Aiba, I., and Shuttleworth, C.W. (2012). Sustained NMDA receptor activation by spreading depolarizations can initiate excitotoxic injury in metabolically compromised neurons. J. Physiol. *590*, 5877–5893.

Aitken, P.G., Breese, G.R., Dudek, F.F., Edwards, F., Espanol, M.T., Larkman, P.M., Lipton, P., Newman, G.C., Nowak, T.S., Jr., Panizzon, K.L., et al. (1995). Preparative methods for brain slices: a discussion. J. Neurosci. Methods *59*, 139–149.

Amzica, F. (2002). In vivo electrophysiological evidences for cortical neuron-glia interactions during slow (<1 Hz) and paroxysmal sleep oscillations. J. Physiol. Paris *96*, 209–219.

Angulo, M.C., Kozlov, A.S., Charpak, S., and Audinat, E. (2004). Glutamate released from glial cells synchronizes neuronal activity in the hippocampus. J. Neurosci. *24*, 6920–6927.

Araque, A., Sanzgiri, R.P., Parpura, V., and Haydon, P.G. (1998a). Calcium elevation in astrocytes causes an NMDA receptor-dependent increase in the frequency of miniature synaptic currents in cultured hippocampal neurons. J. Neurosci. *18*, 6822–6829.

Araque, A., Parpura, V., Sanzgiri, R.P., and Haydon, P.G. (1998b). Glutamate-dependent astrocyte modulation of synaptic transmission between cultured hippocampal neurons. Eur. J. Neurosci. *10*, 2129–2142.

Araque, A., Li, N., Doyle, R.T., and Haydon, P.G. (2000). SNARE protein-dependent glutamate release from astrocytes. J. Neurosci. *20*, 666–673.

Arnth-Jensen, N., Jabaudon, D., and Scanziani, M. (2002). Cooperation between independent hippocampal synapses is controlled by glutamate uptake. Nat. Neurosci. *5*, 325–331.

Ashton, D., Willems, R., Marrannes, R., and Janssen, P.A. (1990). Extracellular ions during veratridine-induced neurotoxicity in hippocampal slices: neuroprotective effects of flunarizine and tetrodotoxin. Brain Res. *528*, 212–222.

Awatramani, G.B., Price, G.D., and Trussell, L.O. (2005). Modulation of transmitter release by presynaptic resting potential and background calcium levels. Neuron *48*, 109–121.

Banerjee, A., Larsen, R.S., Philpot, B.D., and Paulsen, O. (2016). Roles of presynaptic NMDA receptors in neurotransmission and plasticity. Trends Neurosci. *39*, 26–39.

Barthó, P., Payne, J.A., Freund, T.F., and Acsády, L. (2004). Differential distribution of the KCl cotransporter KCC2 in thalamic relay and reticular nuclei. Eur. J. Neurosci. *20*, 965–975.

Basarsky, T.A., Feighan, D., and MacVicar, B.A. (1999). Glutamate release through volume-activated channels during spreading depression. J. Neurosci. *19*, 6439–6445.

Bergles, D.E., and Jahr, C.E. (1997). Synaptic activation of glutamate transporters in hippocampal astrocytes. Neuron *19*, 1297–1308.

Brennan, K.C., and Pietrobon, D. (2018). A systems neuroscience approach to migraine. Neuron *97*, 1004–1021.

Brennan, K.C., Bates, E.A., Shapiro, R.E., Zyuzin, J., Hallows, W.C., Huang, Y., Lee, H.-Y., Jones, C.R., Fu, Y.-H., Charles, A.C., et al. (2013). Casein kinase iδ mutations in familial migraine and advanced sleep phase. Sci. Transl. Med. *5*, 183ra56.

Burstein, R., Noseda, R., and Borsook, D. (2015). Migraine: multiple processes, complex pathophysiology. J. Neurosci. *35*, 6619–6629.

Capuani, C., Melone, M., Tottene, A., Bragina, L., Crivellaro, G., Santello, M., Casari, G., Conti, F., and Pietrobon, D. (2016). Defective glutamate and K+ clearance by cortical astrocytes in familial hemiplegic migraine type 2. EMBO Mol. Med. *8*, 967–986.

Cavelier, P., and Attwell, D. (2007). Neurotransmitter depletion by bafilomycin is promoted by vesicle turnover. Neurosci. Lett. *412*, 95–100.

Chapin, J., and Lin, C. (1990). The somatic sensory cortex of the rat. The Cerebral Cortex of the Rat (MIT Press), pp. 341–380.

Chen, W., Mahadomrongkul, V., Berger, U.V., Bassan, M., DeSilva, T., Tanaka, K., Irwin, N., Aoki, C., and Rosenberg, P.A. (2004). The glutamate transporter GLT1a is expressed in excitatory axon terminals of mature hippocampal neurons. J. Neurosci. *24*, 1136–1148.

Chen, Q., Cichon, J., Wang, W., Qiu, L., Lee, S.-J.R., Campbell, N.R., Destefino, N., Goard, M.J., Fu, Z., Yasuda, R., et al. (2012). Imaging neural activity using Thy1-GCaMP transgenic mice. Neuron *76*, 297–308.

Chen, T.-W., Wardill, T.J., Sun, Y., Pulver, S.R., Renninger, S.L., Baohan, A., Schreiter, E.R., Kerr, R.A., Orger, M.B., Jayaraman, V., et al. (2013). Ultrasensitive fluorescent proteins for imaging neuronal activity. Nature *499*, 295–300.

Chinopoulos, C., Connor, J.A., and Shuttleworth, C.W. (2007). Emergence of a spermine-sensitive, non-inactivating conductance in mature hippocampal CA1 pyramidal neurons upon reduction of extracellular Ca2+: dependence on intracellular Mg2+ and ATP. Neurochem. Int. *50*, 148–158.

Cholet, N., Pellerin, L., Magistretti, P.J., and Hamel, E. (2002). Similar perisynaptic glial localization for the Na+,K+-ATPase alpha 2 subunit and the glutamate transporters GLAST and GLT-1 in the rat somatosensory cortex. Cereb. Cortex *12*, 515–525.

Constantinople, C.M., and Bruno, R.M. (2011). Effects and mechanisms of wakefulness on local cortical networks. Neuron *69*, 1061–1068.

Dana, H., Chen, T.-W., Hu, A., Shields, B.C., Guo, C., Looger, L.L., Kim, D.S., and Svoboda, K. (2014). Thy1-GCaMP6 transgenic mice for neuronal population imaging in vivo. PLoS One *9*, e108697.

Danbolt, N.C. (2001). Glutamate uptake. Prog. Neurobiol. *65*, 1–105.

De Fusco, M., Marconi, R., Silvestri, L., Atorino, L., Rampoldi, L., Morgante, L., Ballabio, A., Aridon, P., and Casari, G. (2003). Haploinsufficiency of ATP1A2 encoding the Na+/K+ pump alpha2 subunit associated with familial hemiplegic migraine type 2. Nat. Genet. *33*, 192–196.

de Vivo, L., Melone, M., Rothstein, J.D., and Conti, F. (2010). GLT-1 promoter activity in astrocytes and neurons of mouse hippocampus and somatic sensory cortex. Front. Neuroanat. *3*, 31.

DeFelipe, J., Marco, P., Busturia, I., and Merchán-Pérez, A. (1999). Estimation of the number of synapses in the cerebral cortex: methodological considerations. Cereb. Cortex *9*, 722–732.

Diamond, J.S., and Jahr, C.E. (1997). Transporters buffer synaptically released glutamate on a submillisecond time scale. J. Neurosci. *17*, 4672–4687.

Dombeck, D.A., Khabbaz, A.N., Collman, F., Adelman, T.L., and Tank, D.W. (2007). Imaging large-scale neural activity with cellular resolution in awake, mobile mice. Neuron *56*, 43–57.

Dreier, J.P., Fabricius, M., Ayata, C., Sakowitz, O.W., Shuttleworth, C.W., Dohmen, C., Graf, R., Vajkoczy, P., Helbok, R., Suzuki, M., et al. (2017). Recording, analysis, and interpretation of spreading depolarizations in neurointensive care: Review and recommendations of the COSBID research group. J. Cereb. Blood Flow Metab. *37*, 1595–1625.

Eikermann-Haerter, K., Dileköz, E., Kudo, C., Savitz, S.I., Waeber, C., Baum, M.J., Ferrari, M.D., van den Maagdenberg, A.M.J.M., Moskowitz, M.A., and Ayata, C. (2009). Genetic and hormonal factors modulate spreading depression and transient hemiparesis in mouse models of familial hemiplegic migraine type 1. J. Clin. Invest. *119*, 99–109.

Eikermann-Haerter, K., Yuzawa, I., Qin, T., Wang, Y., Baek, K., Kim, Y.R., Hoffmann, U., Dilekoz, E., Waeber, C., Ferrari, M.D., et al. (2011). Enhanced subcortical spreading depression in familial hemiplegic migraine type 1 mutant mice. J. Neurosci. *31*, 5755–5763.

Eikermann-Haerter, K., Arbel-Ornath, M., Yalcin, N., Yu, E.S., Kuchibhotla, K.V., Yuzawa, I., Hudry, E., Willard, C.R., Climov, M., Keles, F., et al. (2015). Abnormal synaptic Ca(2+) homeostasis and morphology in cortical neurons of familial hemiplegic migraine type 1 mutant mice. Ann. Neurol. *78*, 193–210.

Emptage, N.J., Reid, C.A., and Fine, A. (2001). Calcium stores in hippocampal synaptic boutons mediate short-term plasticity, store-operated Ca2+ entry, and spontaneous transmitter release. Neuron *29*, 197–208.

Enger, R., Tang, W., Vindedal, G.F., Jensen, V., Johannes Helm, P., Sprengel, R., Looger, L.L., and Nagelhus, E.A. (2015). Dynamics of ionic shifts in cortical spreading depression. Cereb. Cortex *25*, 4469–4476.

Ermolyuk, Y.S., Alder, F.G., Surges, R., Pavlov, I.Y., Timofeeva, Y., Kullmann, D.M., and Volynski, K.E. (2013). Differential triggering of spontaneous glutamate release by P/Q-, N- and R-type Ca2+ channels. Nat. Neurosci. *16*, 1754–1763.

Fekete, A., Franklin, L., Ikemoto, T., Rózsa, B., Lendvai, B., Sylvester Vizi, E., and Zelles, T. (2009). Mechanism of the persistent sodium current activator veratridine-evoked Ca elevation: implication for epilepsy. J. Neurochem. *111*, 745–756.

Fellin, T., Pascual, O., Gobbo, S., Pozzan, T., Haydon, P.G., and Carmignoto, G. (2004). Neuronal synchrony mediated by astrocytic glutamate through activation of extrasynaptic NMDA receptors. Neuron *43*, 729–743.

Fiacco, T.A., and McCarthy, K.D. (2018). Multiple lines of evidence indicate that gliotransmission does not occur under physiological conditions. J. Neurosci. *38*, 3–13.

Gambino, F., Pagès, S., Kehayas, V., Baptista, D., Tatti, R., Carleton, A., and Holtmaat, A. (2014). Sensory-evoked LTP driven by dendritic plateau potentials in vivo. Nature *515*, 116–119.

Gómez-Gonzalo, M., Zehnder, T., Requie, L.M., Bezzi, P., and Carmignoto, G. (2018). Insights into the release mechanism of astrocytic glutamate evoking in neurons NMDA receptor-mediated slow depolarizing inward currents. Glia *66*, 2188–2199.

Helmstaedter, M., Staiger, J.F., Sakmann, B., and Feldmeyer, D. (2008). Efficient recruitment of layer 2/3 interneurons by layer 4 input in single columns of rat somatosensory cortex. J. Neurosci. *28*, 8273–8284.

Hinzman, J.M., DiNapoli, V.A., Mahoney, E.J., Gerhardt, G.A., and Hartings, J.A. (2015). Spreading depolarizations mediate excitotoxicity in the development of acute cortical lesions. Exp. Neurol. *267*, 243–253.

Holtmaat, A., Bonhoeffer, T., Chow, D.K., Chuckowree, J., De Paola, V., Hofer, S.B., Hübener, M., Keck, T., Knott, G., Lee, W.-C.A., et al. (2009). Long-term, high-resolution imaging in the mouse neocortex through a chronic cranial window. Nat. Protoc. *4*, 1128–1144.

Innocenti, B., Parpura, V., and Haydon, P.G. (2000). Imaging extracellular waves of glutamate during calcium signaling in cultured astrocytes. J. Neurosci. *20*, 1800–1808.

Jansen, N.A., Dehghani, A., Linssen, M.M.L., Breukel, C., Tolner, E.A., and van den Maagdenberg, A.M.J.M. (2020). First FHM3 mouse model shows

spontaneous cortical spreading depolarizations. Ann. Clin. Transl. Neurol. *7*, 132–138.

Kaeser, P.S., and Regehr, W.G. (2014). Molecular mechanisms for synchronous, asynchronous, and spontaneous neurotransmitter release. Annu. Rev. Physiol. *76*, 333–363.

Kang, J., Jiang, L., Goldman, S.A., and Nedergaard, M. (1998). Astrocyte-mediated potentiation of inhibitory synaptic transmission. Nat. Neurosci. *1*, 683–692.

Kaufmann, D., Theriot, J.J., Zyuzin, J., Service, C.A., Chang, J.C., Tang, Y.T., Bogdanov, V.B., Multon, S., Schoenen, J., Ju, Y.S., and Brennan, K.C. (2017). Heterogeneous incidence and propagation of spreading depolarizations. J. Cereb. Blood Flow Metab. *37*, 1748–1762.

Kitamura, K., Judkewitz, B., Kano, M., Denk, W., and Häusser, M. (2008). Targeted patch-clamp recordings and single-cell electroporation of unlabeled neurons in vivo. Nat. Methods *5*, 61–67.

Krivánek, J. (1978). A different mode of action of potassium ions and veratridine on the formation of cyclic adenosine monophosphate in the cerebral cortex. Neuroscience *3*, 333–338.

Leao, A.A.P. (1944). Spreading depression of activity in the cerebral cortex. J. Neurophysiol. *7*, 359–390.

Leo, L., Gherardini, L., Barone, V., De Fusco, M., Pietrobon, D., Pizzorusso, T., and Casari, G. (2011). Increased susceptibility to cortical spreading depression in the mouse model of familial hemiplegic migraine type 2. PLoS Genet. *7*, e1002129.

Lindquist, B.E., and Shuttleworth, C.W. (2012). Adenosine receptor activation is responsible for prolonged depression of synaptic transmission after spreading depolarization in brain slices. Neuroscience *223*, 365–376.

Lowery, R.L., and Majewska, A.K. (2010). Intracranial injection of adeno-associated viral vectors. J. Vis. Exp. 2140, https://doi.org/10.3791/2140.

Lujan, R., Nusser, Z., Roberts, J.D., Shigemoto, R., and Somogyi, P. (1996). Perisynaptic location of metabotropic glutamate receptors mGluR1 and mGluR5 on dendrites and dendritic spines in the rat hippocampus. Eur. J. Neurosci. *8*, 1488–1500.

Madisen, L., Garner, A.R., Shimaoka, D., Chuong, A.S., Klapoetke, N.C., Li, L., van der Bourg, A., Niino, Y., Egolf, L., Monetti, C., et al. (2015). Transgenic mice for intersectional targeting of neural sensors and effectors with high specificity and performance. Neuron *85*, 942–958.

Marchetti, C., and Gavazzo, P. (2005). NMDA receptors as targets of heavy metal interaction and toxicity. Neurotox. Res. *8*, 245–258.

Marvin, J.S., Borghuis, B.G., Tian, L., Cichon, J., Harnett, M.T., Akerboom, J., Gordus, A., Renninger, S.L., Chen, T.-W., Bargmann, C.I., et al. (2013). An optimized fluorescent probe for visualizing glutamate neurotransmission. Nat. Methods *10*, 162–170.

McCaslin, A.F.H., Chen, B.R., Radosevich, A.J., Cauli, B., and Hillman, E.M.C. (2011). In vivo 3D morphology of astrocyte-vasculature interactions in the somatosensory cortex: implications for neurovascular coupling. J. Cereb. Blood Flow Metab. *31*, 795–806.

Mehina, E.M.F., Murphy-Royal, C., and Gordon, G.R. (2017). Steady-state free Ca2+ in astrocytes is decreased by experience and impacts arteriole tone. J. Neurosci. *37*, 8150–8165.

Melone, M., Bellesi, M., and Conti, F. (2009). Synaptic localization of GLT-1a in the rat somatic sensory cortex. Glia *57*, 108–117.

Melone, M., Bellesi, M., Ducati, A., Iacoangeli, M., and Conti, F. (2011). Cellular and synaptic localization of EAAT2a in human cerebral cortex. Front. Neuroanat. *4*, 151.

Melone, M., Ciappelloni, S., and Conti, F. (2015). A quantitative analysis of cellular and synaptic localization of GAT-1 and GAT-3 in rat neocortex. Brain Struct. Funct. *220*, 885–897.

Melone, M., Ciriachi, C., Pietrobon, D., and Conti, F. (2019). Heterogeneity of astrocytic and neuronal GLT-1 at cortical excitatory synapses, as revealed by its colocalization with Na+/K+-ATPase α isoforms. Cereb. Cortex *29*, 3331–3350.

Mishima, T., and Hirase, H. (2010). In vivo intracellular recording suggests that gray matter astrocytes in mature cerebral cortex and hippocampus are electrophysiologically homogeneous. J. Neurosci. *30*, 3093–3100.

Ni, Y., and Parpura, V. (2009). Dual regulation of Ca2+-dependent glutamate release from astrocytes: vesicular glutamate transporters and cytosolic glutamate levels. Glia *57*, 1296–1305.

Nieuwenhuys, R. (2013). The myeloarchitectonic studies on the human cerebral cortex of the Vogt-Vogt school, and their significance for the interpretation of functional neuroimaging data. Brain Struct. Funct. *218*, 303–352.

Nimmerjahn, A., and Helmchen, F. (2012). In vivo labeling of cortical astrocytes with sulforhodamine 101 (SR101). Cold Spring Harb. Protoc. *2012*, 326–334.

Nishiyama, N., Colonna, J., Shen, E., Carrillo, J., and Nishiyama, H. (2014). Long-term in vivo time-lapse imaging of synapse development and plasticity in the cerebellum. J. Neurophysiol. *111*, 208–216.

Omrani, A., Melone, M., Bellesi, M., Safiulina, V., Aida, T., Tanaka, K., Cherubini, E., and Conti, F. (2009). Up-regulation of GLT-1 severely impairs LTD at mossy fibre–CA3 synapses. J. Physiol. *587*, 4575–4588.

Perea, G., and Araque, A. (2005). Properties of synaptically evoked astrocyte calcium signal reveal synaptic information processing by astrocytes. J. Neurosci. *25*, 2192–2203.

Perea, G., Yang, A., Boyden, E.S., and Sur, M. (2014). Optogenetic astrocyte activation modulates response selectivity of visual cortex neurons in vivo. Nat. Commun. *5*, 3262.

Peters, A., Palay, S.L., and deF Webster, H. (1991). Fine structure of the nervous system: neurons and their supporting cells (Oxford University Press).

Pietrobon, D. (2007). Familial hemiplegic migraine. Neurotherapeutics *4*, 274–284.

Pietrobon, D. (2013). Calcium channels and migraine. Biochim. Biophys. Acta *1828*, 1655–1665.

Pietrobon, D., and Brennan, K.C. (2019). Genetic mouse models of migraine. J. Headache Pain *20*, 79.

Pietrobon, D., and Moskowitz, M.A. (2014). Chaos and commotion in the wake of cortical spreading depression and spreading depolarizations. Nat. Rev. Neurosci. *15*, 379–393.

Poskanzer, K.E., and Yuste, R. (2011). Astrocytic regulation of cortical UP states. Proc. Natl. Acad. Sci. USA *108*, 18453–18458.

Poskanzer, K.E., and Yuste, R. (2016). Astrocytes regulate cortical state switching in vivo. Proc. Natl. Acad. Sci. USA *113*, E2675–E2684.

Rema, V., Armstrong-James, M., and Ebner, F.F. (1998). Experience-dependent plasticity of adult rat S1 cortex requires local NMDA receptor activation. J. Neurosci. *18*, 10196–10206.

Romanos, J., Benke, D., Pietrobon, D., Zeilhofer, H.U., and Santello, M. (2020). Astrocyte dysfunction increases cortical dendritic excitability and promotes cranial pain in familial migraine. Sci. Adv. *6*, eaaz1584.

Rose, E.M., Koo, J.C.P., Antflick, J.E., Ahmed, S.M., Angers, S., and Hampson, D.R. (2009). Glutamate transporter coupling to Na,K-ATPase. J. Neurosci. *29*, 8143–8155.

Rosenegger, D.G., Tran, C.H.T., Wamsteeker Cusulin, J.I., and Gordon, G.R. (2015). Tonic local brain blood flow control by astrocytes independent of phasic neurovascular coupling. J. Neurosci. *35*, 13463–13474.

Rossi, D.J., Oshima, T., and Attwell, D. (2000). Glutamate release in severe brain ischaemia is mainly by reversed uptake. Nature *403*, 316–321.

Rothstein, J.D., Martin, L., Levey, A.I., Dykes-Hoberg, M., Jin, L., Wu, D., Nash, N., and Kuncl, R.W. (1994). Localization of neuronal and glial glutamate transporters. Neuron *13*, 713–725.

Rothstein, J.D., Dykes-Hoberg, M., Pardo, C.A., Bristol, L.A., Jin, L., Kuncl, R.W., Kanai, Y., Hediger, M.A., Wang, Y., Schielke, J.P., and Welty, D.F. (1996). Knockout of glutamate transporters reveals a major role for astroglial transport in excitotoxicity and clearance of glutamate. Neuron *16*, 675–686.

Rungta, R.L., Choi, H.B., Tyson, J.R., Malik, A., Dissing-Olesen, L., Lin, P.J.C., Cain, S.M., Cullis, P.R., Snutch, T.P., and MacVicar, B.A. (2015). The cellular

mechanisms of neuronal swelling underlying cytotoxic edema. Cell *161*, 610–621.

Sasaki, T., Beppu, K., Tanaka, K.F., Fukazawa, Y., Shigemoto, R., and Matsui, K. (2012). Application of an optogenetic byway for perturbing neuronal activity via glial photostimulation. Proc. Natl. Acad. Sci. USA *109*, 20720–20725.

Savić, N., and Sciancalepore, M. (1998). Intracellular calcium stores modulate miniature GABA-mediated synaptic currents in neonatal rat hippocampal neurons. Eur. J. Neurosci. *10*, 3379–3386.

Savtchouk, I., and Volterra, A. (2018). Gliotransmission: Beyond Black-and-White. J. Neurosci. *38*, 14–25.

Sawant-Pokam, P.M., Suryavanshi, P., Mendez, J.M., Dudek, F.E., and Brennan, K.C. (2017). Mechanisms of neuronal silencing after cortical spreading depression. Cereb. Cortex *27*, 1311–1325.

Schindelin, J., Arganda-Carreras, I., Frise, E., Kaynig, V., Longair, M., Pietzsch, T., Preibisch, S., Rueden, C., Saalfeld, S., Schmid, B., et al. (2012). Fiji: an open-source platform for biological-image analysis. Nat. Methods *9*, 676–682.

Schneggenburger, R., and Rosenmund, C. (2015). Molecular mechanisms governing Ca(2+) regulation of evoked and spontaneous release. Nat. Neurosci. *18*, 935–941.

Schneider, C.A., Rasband, W.S., and Eliceiri, K.W. (2012). NIH Image to ImageJ: 25 years of image analysis. Nat. Methods *9*, 671–675.

Sharma, G., and Vijayaraghavan, S. (2003). Modulation of presynaptic store calcium induces release of glutamate and postsynaptic firing. Neuron *38*, 929–939.

Shuttleworth, C.W., Brennan, A.M., and Connor, J.A. (2003). NAD(P)H fluorescence imaging of postsynaptic neuronal activation in murine hippocampal slices. J. Neurosci. *23*, 3196–3208.

Somjen, G.G. (2001). Mechanisms of spreading depression and hypoxic spreading depression-like depolarization. Physiol. Rev. *81*, 1065–1096.

Srinivasan, R., Lu, T.-Y., Chai, H., Xu, J., Huang, B.S., Golshani, P., Coppola, G., and Khakh, B.S. (2016). New transgenic mouse lines for selectively targeting astrocytes and studying calcium signals in astrocyte processes in situ and in vivo. Neuron *92*, 1181–1195.

Suryavanshi, P., Pokam, P.S., and Brennan, K.C. (2019). Altered synaptic adaptation and gain in sensory circuits of the casein kinase 1 delta (CK1dT44A) mouse model of migraine. bioRxiv. https://doi.org/10.1101/719039.

Tanaka, K., Watase, K., Manabe, T., Yamada, K., Watanabe, M., Takahashi, K., Iwama, H., Nishikawa, T., Ichihara, N., Kikuchi, T., et al. (1997). Epilepsy and exacerbation of brain injury in mice lacking the glutamate transporter GLT-1. Science *276*, 1699–1702.

Tang, Y.T., Mendez, J.M., Theriot, J.J., Sawant, P.M., López-Valdés, H.E., Ju, Y.S., and Brennan, K.C. (2014). Minimum conditions for the induction of cortical spreading depression in brain slices. J. Neurophysiol. *112*, 2572–2579.

Theriot, J.J., Toga, A.W., Prakash, N., Ju, Y.S., and Brennan, K.C. (2012). Cortical sensory plasticity in a model of migraine with aura. J. Neurosci. *32*, 15252–15261.

Tottene, A., Moretti, A., and Pietrobon, D. (1996). Functional diversity of P-type and R-type calcium channels in rat cerebellar neurons. J. Neurosci. *16*, 6353–6363.

Tottene, A., Conti, R., Fabbro, A., Vecchia, D., Shapovalova, M., Santello, M., van den Maagdenberg, A.M.J.M., Ferrari, M.D., and Pietrobon, D. (2009). Enhanced excitatory transmission at cortical synapses as the basis for facilitated spreading depression in Ca(v)2.1 knockin migraine mice. Neuron *61*, 762–773.

Tottene, A., Urbani, A., and Pietrobon, D. (2011). Role of different voltage-gated Ca2+ channels in cortical spreading depression: specific requirement of P/Q-type Ca2+ channels. Channels (Austin) *5*, 110–114.

Tran, C.H.T., Peringod, G., and Gordon, G.R. (2018). Astrocytes integrate behavioral state and vascular signals during functional hyperemia. Neuron *100*, 1133–1148.e3.

Tsukada, S., Iino, M., Takayasu, Y., Shimamoto, K., and Ozawa, S. (2005). Effects of a novel glutamate transporter blocker, (2S, 3S)-3-[3-[4-(trifluoromethyl)benzoylamino]benzyloxy]aspartate (TFB-TBOA), on activities of hippocampal neurons. Neuropharmacology *48*, 479–491.

Ulbricht, W. (2005). Sodium channel inactivation: molecular determinants and modulation. Physiol. Rev. *85*, 1271–1301.

van den Maagdenberg, A.M.J.M., Pietrobon, D., Pizzorusso, T., Kaja, S., Broos, L.A.M., Cesetti, T., van de Ven, R.C.G., Tottene, A., van der Kaa, J., Plomp, J.J., et al. (2004). A Cacna1a knockin migraine mouse model with increased susceptibility to cortical spreading depression. Neuron *41*, 701–710.

van den Maagdenberg, A.M.J.M., Pizzorusso, T., Kaja, S., Terpolilli, N., Shapovalova, M., Hoebeek, F.E., Barrett, C.F., Gherardini, L., van de Ven, R.C.G., Todorov, B., et al. (2010). High cortical spreading depression susceptibility and migraine-associated symptoms in Ca(v)2.1 S218L mice. Ann. Neurol. *67*, 85–98.

Vandenberg, R.J., and Ryan, R.M. (2013). Mechanisms of glutamate transport. Physiol. Rev. *93*, 1621–1657.

Vogt, B.A. (1991). The role of layer I in cortical function. In Normal and Altered States of Function, A. Peters and E.G. Jones, eds. (Springer US), pp. 49–80.

Wang, Y., DelRosso, N.V., Vaidyanathan, T.V., Cahill, M.K., Reitman, M.E., Pittolo, S., Mi, X., Yu, G., and Poskanzer, K.E. (2019). Accurate quantification of astrocyte and neurotransmitter fluorescence dynamics for single-cell and population-level physiology. Nat. Neurosci. *22*, 1936–1944.

Wu, D.C., Chen, R.Y.-T., Cheng, T.-C., Chiang, Y.-C., Shen, M.-L., Hsu, L.-L., and Zhou, N. (2018). Spreading depression promotes astrocytic calcium oscillations and enhances gliotransmission to hippocampal neurons. Cereb. Cortex *28*, 3204–3216.

Xie, Y., Chan, A.W., McGirr, A., Xue, S., Xiao, D., Zeng, H., and Murphy, T.H. (2016). Resolution of high-frequency mesoscale intracortical maps using the genetically encoded glutamate sensor iGluSnFR. J. Neurosci. *36*, 1261–1272.

Xu, N.L., Harnett, M.T., Williams, S.R., Huber, D., O'Connor, D.H., Svoboda, K., and Magee, J.C. (2012). Nonlinear dendritic integration of sensory and motor input during an active sensing task. Nature *492*, 247–251.

Zamponi, G.W., Bourinet, E., and Snutch, T.P. (1996). Nickel block of a family of neuronal calcium channels: subtype- and subunit-dependent action at multiple sites. J. Membr. Biol. *151*, 77–90.

Zhou, N., Rungta, R.L., Malik, A., Han, H., Wu, D.C., and MacVicar, B.A. (2013). Regenerative glutamate release by presynaptic NMDA receptors contributes to spreading depression. J. Cereb. Blood Flow Metab. *33*, 1582–1594.

STAR★METHODS

KEY RESOURCES TABLE

REAGENT or RESOURCE	SOURCE	IDENTIFIER
Antibodies		
Rabbit polyclonal anti-cGLT1a	Chen et al., 2004; Rothstein et al., 1994	RRID:AB_2314565
Goat anti-rabbit biotinylated	Jackson ImmunoResearch Europe Inc.	Catalog # 111-065-144; RRID:AB_2337965
Donkey anti-rabbit Alexa Fluor 488-conjugated	Jackson ImmunoResearch Europe Inc.	Catalog #711-006-152; RRID: AB_2340619
Bacterial and virus strains		
AAV1.hSyn.iGluSnFr.WPRE.SV40	Marvin et al., 2013; UPenn Vector Core	AV-1-PV2723
Chemicals, peptides, and recombinant proteins		
((3S)-3-[[3-[[4-(Trifluoromethyl)benzoyl]amino]phenyl] methoxy]-L-aspartic acid (TFB-TBOA)	Tocris	Catalog #: 2532
Tetrodotoxin (TTX)	Tocris	Catalog #: 1078
Nickel(II) chloride	Sigma-Aldrich	Catalog #: 339350
Veratridine	Tocris	Catalog #: 2918
Bafilomycin A1 (BafA1)	Enzo Life Sciences	Catalog #: BML-CM110-0100
Sulforhodamine 101 (SR101)	Sigma-Aldrich	Catalog #: S7635
Thapsigargin	Sigma-Aldrich	Catalog #: T9033
DL-2-Amino-5-phosphonopentanoic acid (DL-APV)	Tocris	Catalog #: 0105
6,7-Dinitroquinoxaline-2,3-dione disodium salt (DNQX)	Tocris	Catalog #: 2312
3-((2-Methyl-1,3-thiazol-4-yl)ethynyl)pyridine hydrochloride (MTEP)	Tocris	Catalog #: 2921
6-Methoxy-N-(4-methoxyphenyl)-4-quinazolinamine hydrochloride (LY 456236)	Tocris	Catalog #: 2390
Experimental models: organisms/strains		
FHM2 (*Atp1a2*$^{+/R887}$) knock-in mice	Leo et al., 2011	N/A
Thy1-GCaMP6s mice [C57BL/6J-Tg(Thy1-GCaMP6s) GP4.3Dkim/J]	Dana et al., 2014; Jackson Laboratory	Stock #: 024275
Aldh1l1-Cre mice [B6;FVB-Tg(Aldh1l1-cre/ERT2) 1Khakh/J]	Srinivasan et al., 2016; Jackson Laboratory	Stock #: 029655
Ai96 mice [B6;129S6-Gt(ROSA)26Sortm96(CAG-GCaMP6s)Hze/J]	Madisen et al., 2015; Jackson Laboratory	Stock #: 024106
C57BL/6J mice	Jackson Laboratory	Stock #: 000664
Software and algorithms		
MATLAB $\geq$ 2014a	Mathworks	https://www.mathworks.com/
Prism	Graphpad	https://www.graphpad.com/
Fiji	Schindelin et al., 2012; ImageJ	https://imagej.net/Welcome

RESOURCE AVAILABILITY

Lead contact

Further information and requests for resources and reagents should be directed to and will be fulfilled by the Lead Contact, K.C. Brennan (k.c.brennan@hsc.utah.edu).

Materials availability

This study did not generate new unique reagents.

Data and code availability

The datasets and code supporting the current study have not been deposited in a public repository but are available from the lead contact on request.

EXPERIMENTAL MODEL AND SUBJECT DETAILS

All experiments were conducted in accordance with and approved by governing bodies at respective universities (University of Utah and the University of New Mexico Health Sciences Center: U.S. National Institute of Health's *Guide for the Care and Use of Laboratory Animals* and Institutional Animal Care and Use Committees; Università Politecnica delle Marche: Italian National (D.L. n.26, March 14, 2014) and European Community Council (2010/63/UE) and were approved by the local veterinary service). Experiments used adult heterozygous male and female FHM2 knock-in mice (*Atp1a2*$^{+/R887}$) and WT littermates (*Atp1a2*$^{+/+}$) as controls (3 – 6 months of age) (Leo et al., 2011). We did not see a significant difference in baseline plume frequency in male and female FHM2 mice across our experiments, though there was a trend toward a lower frequency of plumes in females [females = 0.95 (0.17 2.50) plumes/min, n = 13 mice; males = 2.09 (0.62 3.43), n = 21; p = 0.16, Wilcoxon rank sum; median (Q1 Q3)]. TTX control and neural Ca^{2+} plume experiments used Thy1-GCaMP6s mice [C57BL/6J-Tg(Thy1-GCaMP6s)GP4.3Dkim/J] (Dana et al., 2014) crossed with our FHM2 mouse line (FHM2.Thy1-GCaMP6s mice). Astrocyte Ca^{2+} recordings were performed in Aldh1l1-Cre/ERT2 mice [B6;FVB-Tg(Aldh1l1-cre/ERT2)1Khakh/J] (Srinivasan et al., 2016) crossed with Ai96 mice [B6;129S6-Gt(ROSA)26Sortm96(CAG-GCaMP6s)Hze/J] (Madisen et al., 2015) to express GCaMP6s specifically in astrocytes. Hippocampal experiments were performed in C57BL/6J mice (7-11 weeks, both sexes). Electron microscopy (EM) experiments used two FHM2 and two WT (1 male and 1 female from each genotype; P34-P35). Immunofluorescence used two WT (1 male, 1 female) P35-40 mice. Animals were housed in a temperature and humidity-controlled vivarium with a 12-hour light/dark cycle with free access to food and water. Mice used for physiology experiments underwent a prior viral injection surgery (see Viral injections below), and all animals recovered and were in good health at the time of recording.

METHOD DETAILS

Experimental design

Sample size was based on previous reports, generally n = 6 – 9 for *in vivo* and *in vitro* experiments. In some instances, data collection was stopped early due to clear phenotypes. Experimenters were blinded in all EM experiments, and in physiology experiments when genotypes were compared. However, many physiology experiments focused on drug conditions in FHM2 mice using a within-subjects experimental design, where recordings were always performed first with a vehicle solution ('baseline'), followed by a drug solution, to avoid additional confounds related to irreversible or continued effects of drugs. When possible, those performing analysis were blinded to experimental conditions, though in some instances, differences in plume characteristics between conditions were so large that the experiments essentially unblinded themselves. Mice with iGluSnFR expression levels too low to record a whisker mediated response or no expression in putative L1a were excluded from experiments (see Fluorescent glutamate analysis section below). Outliers were determined empirically based on data distribution (Grubbs' test) and excluded from statistical analysis and figures. Most comparisons were made either across genotypes within the same condition or across conditions within the same animal (repeated-measures), superseding the need for randomization, except *in vitro* slice experiments, where we interleaved and matched the number of slices to control or experimental conditions from the same animal. When feasible, we replicated findings across different experimental paradigms (e.g., *in vitro* and *in vivo*).

Viral injections

iGluSnFR expression was targeted to neurons in L2/3 barrel cortex and hippocampus using adeno associated virus injections 2 – 3 weeks prior to imaging (AAV1.hSyn.iGluSnFr.WPRE.SV40 (Marvin et al., 2013); Penn Vector Core, catalog #: AV-1-PV2723; $1.3 – 3.8 \times 10^{12}$ GC). For dendrite Ca^{2+} recordings (Figure S4I), GCaMP6f was sparsely expressed in L2/3 neurons of the barrel cortex by co-injecting Cre and Flex.GCaMP6f viruses at a ratio of ~1:10,000 GC, respectively (AAV1.hSyn.Cre.WPRE.hGH and AAV1.CAG.-Flex.GCaMP6f.WPRE.SV40; Penn Vector Core) (Gambino et al., 2014; Xu et al., 2012). Animals were anesthetized using isoflurane and fixed in a stereotaxic frame (4 – 5% induction, 1.5 – 1.75% for surgery; David Kopf Instruments, Models 962, 923B). Bupivacaine (30 μl, subcutaneous) was administered as a local anesthetic and Rimadyl (5 mg/kg, subcutaneous) for postoperative analgesia. Injections were performed using standard sterile practices through a small bur hole using a pulled glass micropipette (Lowery and Majewska, 2010) at coordinates relative to bregma: *Posterior barrel cortex*: right hemisphere injections at −2 mm posterior, +3.4 mm lateral, 200 μm depth, 500 – 750 nL 2P, ≤ 1 μl epifluorescence, at ~50 - 100 nl/min. *Central barrel cortex* (for dendrite imaging): right hemisphere injections at −1 mm posterior, 3.4 mm lateral, 250 μm depth, total volume ~50 nl. *Hippocampus*: bilateral injections at −2.45 mm, +2.3 mm lateral,1.65 mm depth, 500 nl, at ~100 nl/min using a 5.0 μl Hamilton gastight syringe (Hamilton Company Inc., Reno, NV, USA) connected via polyethylene tubing to a 33G diameter infusion cannula (C315I/SPC; Plastics One Inc., Roanoke, VA, USA). For hippocampal injections topical, lidocaine was applied over the incision site and a 40% buprenorphine (0.1 mg/kg) saline

solution was administered intraperitoneally for postoperative pain. Following all injection surgeries, incisions were sutured close and animals recovered on top of a heating pad and were returned to their home cage. Mice were typically housed with 1 – 2 siblings post-surgery, though occasionally were singly housed.

Surgery for awake imaging

Surgical window implantation for *in vivo* imaging was performed the day of recording and used a circular craniotomy (~2.5 mm diameter) implanted anterior to the injection site to reduce damage to the dura and underlying cortex when removing the skull (Holtmaat et al., 2009). Dexamethasone (2 μl at 4 mg/ml, intramuscular) was administered to reduce cerebral edema. The brain was covered with melted agarose (1.2% in saline) and sealed with a circular coverslip (Warner Instruments #1, 3 mm) affixed to the skull with cyanoacrylate glue and dental cement (Stoelting #51458 & 51456). A stainless steel omega bar was cemented to the interparietal bone, and exposed skull and scalp margins were sealed with cement. In a subset of experiments, the skull was thinned over the barrel cortex rather than removed (3 mm x 3 mm square) (Figure S1; Kaufmann et al., 2017).

Perforated coverslips

In vivo pharmacology experiments used a 3 mm diameter circular craniotomy and omitted the agarose, allowing placement of a custom perforated coverslip inside the craniotomy and directly on the dura (Holtmaat et al., 2009; Nishiyama et al., 2014; Tran et al., 2018). Perforated coverslips were made by hand with a dental drill (Neoburr #7901), drilling at a ~35° angle relative to the surface of the coverslip to prevent air being trapped inside the holes during imaging. Holes were cut into a hexagonal shape with one additional hole in the center (7 total; ~200 – 300 μm diameter prevented herniation). Experiments investigating the pharmacology of plumes *in vivo* always used coverslips with 7 holes arranged in the same hexagonal array (TFB-TBOA, TTX, Ni^{2+}, veratridine, thapsigargin, and glutamate receptor inhibitors). SD induction experiments used a single hole near the center of the coverslip to restrict the location of SD initiation. Pilot experiments found that the number of holes in the coverslip influenced SD threshold, likely due to differences in the amount of exposed tissue and diffusion of the drug into the cortex (data not shown) (Tang et al., 2014). For this reason, experiments investigating SD initiation always used coverslips with a single hole (veratridine, veratridine + Ni^{2+}, and KCl). For Ni^{2+} experiments using 1 mM *in vivo*, the dura was removed to increase diffusion of the drug into the brain (Figure 4). For Ni^{2+} experiments using 10 mM to inhibit SD initiation *in vivo*, the dura was left intact so that results would be more comparable to other SD induction experiments (hence, in part, the increase in concentration) (Figure 5).

In vivo awake recording trials

Mice were head fixed to a metal frame atop a floating polystyrene ball and allowed to 'ambulate' similar to a spherical treadmill for 2P and epifluorescence imaging (Dombeck et al., 2007). For 2P, animals were transferred directly to the microscope following surgical window implantation and allowed to acclimate for 1 hour before imaging. For epifluorescence, mice were transferred to their home cage for 2 - 3 hours, then to the microscope for an additional 1 hour. At < 3 hours after anesthetic recovery, whisker mediated glutamate responses were inconsistent across animals. Plumes were still present in FHM2 mice $\geq$ 4.5 – 6 hours post-surgery (Figure 4C). Locomotion and behavior were monitored using an infrared light and webcam with an infrared filter (Virtualdub software). Two-photon recording trials lasted 32.28 – 33.78 s (500 frames at 15.45 Hz sampling rate or 200 frames at 5.92 Hz). *In vivo* epifluorescence trials were 8 s to mitigate bleaching. Whisker stimulation used puffs of air deflecting all whiskers and whisker pad (World Precision Instruments PV830 Pneumatic PicoPump; 40 psi; stimulator placed parallel to the snout, just posterior to the plane of the nose). A single, 40 ms stimulus administered to inactive mice (not running, whisking or grooming) was used to measure clearance kinetics. Under two-photon, plumes were recorded in periods without whisker stimulation, interspersed with stimulation trials using different protocols (40 ms at 1 Hz for 1 s; 40 ms at 10 Hz for 1 s; 400 ms at 1 Hz for 1 – 4 s). There was no difference in the frequency of plumes in trials with or without whisker stimulation (Figure S1G), so plume frequencies were averaged over all trial types.

In vivo optical recording

2P used the following two microscopes:

1. Sutter Movable Objective Microscope with two Hamamatsu R6357 photomultiplier tubes; Zeiss 20x/1.0 NA water-immersion objective; Spectra Physics MaiTai Titanium:Sapphire laser, pulse width ≈100 fs, excitation 920 nm, emission 535/50 nm green, 617/75 nm red; 10 – 20 mW; field of view 384 μm^2 at 1.5 – 3 μm/pixel; image acquisition 2.96 – 5.92 Hz.
2. Neurolabware with Hamamatsu H11901 and H10770B photomultiplier tubes; Cambridge Technology CRS8 8KHz resonant scanning mirror and 6215H galvanometer scanning mirror; Nikon 16x/0.8 NA objective; Coherent Cameleon Discovery dual laser system [tunable laser = 920 nm; fixed laser = 1040 nm; pulse width ≈100 fs]; Semrock emission filters [510/84 nm green & 607/70 nm red]; power ≤ 25 mW; 250 μm – 1.5 mm field of view (FOV) on its long axis at 0.3 – 2 μm/pixel resolution; image acquisition 15.49 Hz; Scanbox acquisition software.

In vivo epifluorescence: SciMedia MiCAM02 12-bit charge-coupled device (CCD) camera; ThorLabs LED #MCWHL2-C1; 360 μm x 250 μm FOV; image acquisition 500 Hz. Performed through the Sutter Movable Objective Microscope.

In vivo electrophysiology

LFP/DC recordings

Silver wire electrodes (A-M Systems, #787000) were coated in Cl^- by soaking in bleach, rinsed, placed in the brain through a small bur hole in the skull, and cemented to the bone during cranial window implantation surgery. Recording electrode was place ipsilateral to imaging window near lambda, while the reference electrode was contralateral, anterior to bregma (depth ~200 μm for both electrodes). Signals were amplified using Brownlee Precision amplifier (model 440), sampled at 1 kHz (bandpass 0 – 300 Hz and notch filtered at 60 Hz) and recorded with Labview. Direct current (DC) was extracted using a lowpass filter $\leq$ 0.1 Hz post hoc in MATLAB.

Astrocyte stimulation and whole-cell recordings in anesthetized mice

Mice were anesthetized throughout the recording with either isoflurane (1 – 1.2%) or urethane (1.5 g/kg administered intraperitoneal) (Kitamura et al., 2008) supplemented with isoflurane (~0.5%), if necessary. A patch electrode (4-6 MΩ resistance) was inserted through intact dura matter while keeping positive pressure (20 kPa) to prevent clogging of the electrode tip. In every recording, viability was verified by ensuring constant values for access resistance (less than 20% variation), or the recording was discarded. Internal solution was (in mM; pH = 7.2): 135 K^+-gluconate, 8 NaCl, 10 HEPES, 0.3 GTP, 2 ATP, 7 phosphocreatine, and 50 μM Alexa Fluor 594. In addition, we added 2 μM Ca^{2+} with no EGTA to the internal solution to assess the role of astrocyte Ca^{2+} in plumes. Astrocytes within the upper portion of L1 were visualized using SR101 perfused over the cortex for ~one minute (Nimmerjahn and Helmchen, 2012). All the astrocytes studied were 30 – 40 μm beneath the brain surface, as very few astrocyte somas are visible in the more superficial parenchyma using SR101 (Figure S2; McCaslin et al., 2011). Signals were amplified using a Multiclamp 700B amplifier (Axon Instruments, Foster city, CA), sampled at 10 kHz (Digidata-1320A), and recorded (pClamp 8.2). We mechanically stimulated astrocytes by touching the soma with the tip of a patch pipette. For mechanical stimulation, a gentle negative pressure was applied for ~1 s onto the astrocyte membrane; the microelectrode was sealed to the cell membrane with a resistance of 40-100 MΩ. Once the whole-cell configuration was achieved, we injected trains of depolarizing current (500–1,000 pA, 500 ms, 10 times) into individual astrocytes that lasted for ~5 s (Poskanzer and Yuste, 2011).

In vivo pharmacology

See Key resources table. Compounds were dissolved in dimethyl sulfoxide (DMSO; Sigma-Aldrich # 472301), then diluted into either physiological saline (*in vivo*) or aCSF (*in vitro*). *In vivo* solutions were based in saline, as aCSF pH quickly increases without oxygen (data not shown). Control solutions contained identical DMSO concentrations to respective drug solutions (all $\leq$ 1%). Ni^{2+} stock was maintained in deionized water. Solutions were exchanged every 30 minutes (Xie et al., 2016). Baseline recordings were performed in control solutions, then removed before manually pipetting drug solutions into the imaging well. Most drug solutions were allowed to superfuse into the underlying cortex for 30 min and maintained during recordings. Ni^{2+} was recorded after 20 min superfusion. For investigating plume mechanisms (Figures 4 and S4), veratridine (100 – 150 μM) was superfused for 10 min, then removed for recording to minimize potential effects of neural swelling (Rungta et al., 2015) and prevent SD induction (see below for the use of veratridine for SD induction). Recordings with thapsigargin were performed during the first 10 min of application, as some previous reports have found that the thapsigargin-induced increase of EPSCs is transient (Sharma and Vijayaraghavan, 2003). A cocktail of glutamate receptor (GluR) inhibitors were combined into a single solution before superfusing into the cortex [DNQX (500 μM) (Tran et al., 2018); MTEP (500 μM); LY 456236 (200 μM); DL-APV (1 mM) (Gambino et al., 2014; Rema et al., 1998; Tran et al., 2018)]. Concentrations for MTEP and LY 456236 used *in vivo* were estimated from *in vitro* experiments, where concentrations similar to DNQX are effective (Mehina et al., 2017; Rosenegger et al., 2015). For SD induction (see below), veratridine or veratridine + Ni^{2+} were maintained in the well during recording. For Ni^{2+} during SD induction, the saline solution was oxygenated (95% O_2/5% CO_2) for 45 min before adding Ni^{2+} (12 mM) to oxygenate for > 30 min. The oxygenated Ni^{2+} 12 mM stock was then added to saline with veratridine (at varied concentrations), with a final Ni^{2+} concentration of 10 mM for experiments. Control solutions contained veratridine in oxygenated saline.

In vivo recording of SD initiation

SD was induced using increasing concentrations of veratridine or KCl through an implanted coverslip with a single perforation. Glutamate fluorescence was recorded using 2P at the surface of the brain inside and adjacent to the fenestration. Veratridine induced SD experiments used simultaneous DC recordings. Veratridine concentrations were increased every 10 min for 0, 100, 300, and 500 μM. This was sufficient to induce SD in all FHM2 (except those with Ni^{2+}). For WT, 750 μM was maintained for 15 – 30 min. Two WT mice required higher concentrations of veratridine, applied at 1, 1.5, 2 and 3 mM increased every 10 min. FHM2 experiments with Ni^{2+} used the same concentrations of veratridine as described for WT above, though 750 μM was only maintained for 10 min. KCl induction experiments in WT used concentrations of 3 (baseline), 150, 275, and 300 mM increased every 10 min until SD induction. We started with a concentration of KCl at 150 mM, because this concentration was unable to induce SD with our focal induction method (a single hole in the coverslip), even when superfused for 45 min in pilot experiments (data not shown) (Tang et al., 2014). However, 150 mM KCl increased the frequency of plumes relative to baseline (3 mM) in all mice ($p = 0.016$; Data S1).

In vivo recording of SD propagation

A small burr hole was made in the skull ipsilateral to the imaging window near lambda. KCl (1 M) was superfused during imaging to induce a single SD several mm from the imaging window, ensuring recording of SD propagation. If more than one SD was induced, only the first SD was included in this study.

Brain slice preparation

Barrel cortex

Animals were deeply anesthetized with 4% isoflurane, decapitated and the brain removed for slice preparation. Coronal sections were cut in ice cold dissection buffer containing (in mM): 220 Sucrose, 3 KCl, 10 $MgSO_4$, 1.25 NaH_2PO_4, 25 $NaHCO_3$, 25 D-glucose, and 0.2 $CaCl_2$. Sections containing somatosensory cortex (Helmstaedter et al., 2008) were allowed to recover in a chamber in aCSF containing (in mM): 125 NaCl, 3 KCl, 1.3 $MgSO_4$, 1.25 NaH_2PO_4, 25 $NaHCO_3$, 25 D-glucose, 1.3 $CaCl_2$, and saturated with 95%O_2 / 5%CO_2, maintained at 35°C.

Hippocampus

As in Shuttleworth et al. (2003), animals were deeply anesthetized with 0.15 mL (s.c) ketamine-xylazine mixture (85 and 15 mg/ml, respectively) and decapitated. Brains were removed quickly into 150 mL oxygenated (95% O_2/5% CO_2) cutting solution containing (in mM): sucrose, 220; $NaHCO_3$, 26; KCl, 3; NaH_2PO_4, 1.5; $MgSO_4$, 6; glucose, 10; $CaCl_2$ 0.2 mL ketamine (100mg/ml, Putney Inc., Portland, ME), to minimize excitotoxicity during the slice preparation (see Aitken et al., 1995). Brains were cut at the coronal orientation into 350 μm cortico-hippocampal slices using a Pelco 102 Vibratome (Ted Pella, Inc., Redding, CA). Slices were then hemisected and allowed to recover at 35°C for 60 min in aCSF containing (in mM): NaCl, 126; $NaHCO_3$, 26; glucose, 10; KCl, 3; $CaCl_2$, 2, NaH_2PO_4, 1.5; $MgSO_4$, 1; equilibrated with 95% O_2/ 5% CO_2. After 1h, the holding aCSF was replaced with 20°C aCSF and slices were left to equilibrate to room temperature until the start of recording sessions. For all slice experiments, the sections were transferred to a submerged chamber constantly supplied with aCSF (flow rate: 2.2 – 2.5 mL/min, saturated with 95%O_2 / 5%CO_2) and maintained at 32° – 35°C (hippocampus and barrel cortex, respectively).

In vitro optical recording

Barrel cortex slice epifluorescence

Acute slices were illuminated by blue light (excitation filter: 420-495nm) and green fluorescence signal (emission filter 520-570nm) was focused on a high-sensitivity 8-bit CCD camera (Mightex CCE-B013-U, Pleasanton, CA, USA) using an upright microscope (Zeiss Axioskop 2) with a 4x/0.10 lens system.

Hippocampal slice transillumination

Slices equilibrated for 10 minutes prior to imaging trials at a bath temperature of 32°C, maintained by an inline heater assembly (TC-344B, Warner Instruments). iGluSnFR was excited at approximately 6Hz (165ms interval) with a 150 W Xenon lamp at 480nm using a monochromator (Polychrome V, Till Photonics GmBH, NY) and imaged using a 10x water-immersion objective (Olympus, 0.3 NA). Fluorescence signals were recorded using a cooled CCD camera (Imago, Till Photonics GmBH) controlled by TillVision version 4.01 software (Till Photonics GmBH). Each imaging trial (300 frames, 49.5 s) was collected in TillVision.

In vitro electrophysiology

Neuronal whole-cell patch-clamp in barrel cortex

Whole-cell patch-clamp recordings were in regular spiking pyramidal neurons in L2/3 somatosensory cortex (Sawant-Pokam et al., 2017). Neurons were visualized using differential interference contrast (DIC) microscopy and patched using glass micropipettes (4-6 MOhms resistance, tip size of 3-4 μm). Spontaneous excitatory post-synaptic currents (EPSCs) were recorded in voltage clamp mode (Vclamp = −70mV) using glass micropipettes filled with intracellular solution containing (in mM; pH = 7.2): 130 $CsMeSO_4$, 3 CsCl, 10 HEPES, 2 MgATP, 0.3 Na3GTP, 5 EGTA, 10 phosphocreatine, 5 QX-314, 8 biocytin, acquired at 20kHz and filtered at 2kHz (lowpass) using Axopatch 700B amplifier. Analog data were digitized using Digidata 1330 digitizer and clampex 9 software (Axon Instruments). Access resistance was monitored throughout recordings (5mV pulses at 50Hz). Recordings with access resistance higher than 25 MOhms or with > 20% change in the access resistance were discarded from analysis. 70% series resistance compensation was applied to recorded currents in voltage clamp setting.

Hippocampal EPSP

Extracellular analog recordings were amplified and digitized with a MultiClamp 700A amplifier (CV-7A headstage) and Digidata 1332A, respectively (Axon Instruments, Molecular Devices) for acquisition (1-10 kHz) by pCLAMP10.2 software (Molecular Devices, LLC, San Jose, CA, USA). Glass recording microelectrodes were filled with aCSF (tip resistance ~3MΩ) and positioned a depth of 50 –100 μm in CA1 stratum radiatum. Excitatory postsynaptic potentials (EPSPs) were evoked using a concentric bipolar electrode (CBAPC74, FHC, Bowdoin, NE, USA) driven by a current controller (A.M.P.I., Jerusalem, Israel) and positioned ~200 μm from the recording electrode for stimulation of Schaffer Collateral inputs using a paired-pulse protocol (2 × 70 μs; interpulse interval of 50ms). After placement of electrodes, input-output curves were generated and current pulses (25-150 μA, 0.1 Hz) were utilized to evoke EPSPs at 40%–60% of maximum amplitude responses.

In vitro pharmacology

Barrel cortex slices

To block vesicular release of glutamate, acute slices were pre-treated with either 4 μM bafilomycin A1 (+BafA1) or vehicle (-BafA1) for 2.5 hr (Agarwal et al., 2017; Cavelier and Attwell, 2007) using micro-perfusion chambers prepared from organotypic slice culture inserts (24mm, Corning) filled with 3mL aCSF (with drug or vehicle) saturated with 95%O_2 / 5%CO_2, maintained at 35°C. Slices were transferred to chambers containing veratridine (10 μM) with BafA1 (+BafA1+Verat.) or without (control group; -BafA1+Verat.) for 5 min to promote turnover of already filled vesicles, then transferred to the recording chamber. BafA1 or control solution (aCSF) were continually recirculated during recording.

Hippocampal slices

After brain slice equilibration in the recording chamber, an initial imaging trial (baseline, 0 min) was collected and subsequent imaging trials were initiated at 5-minute intervals. After baseline acquisition, aCSF containing TFB-TBOA commenced and was maintained throughout the remainder of the experiment. In experiments examining extracellular Ca^{2+} on plume frequency, Ca^{2+} removal (without the addition of chelators) was accompanied by equimolar replacement of extracellular Mg^{2+} (3mM) to maintain extracellular divalent cations resulting in nominally Ca^{2+} - free aCSF (here called 0 Ca^{2+}-aCSF). This equimolar replacement results in < 10μM extracellular Ca^{2+} and prevents the emergence of spermine-sensitive non-inactivating conductance observed in CA1 pyramidal cells upon extracellular Ca^{2+} reduction (Chinopoulos et al., 2007).

GLT-1a Immunofluorescence

Mice were anesthetized with an intraperitoneal injection of chloral hydrate (300 mg/kg) and perfused transcardially with a flush of saline solution followed by 4% freshly depolimerized paraformaldehyde in 0.1 M phosphate buffer (PB; pH 7.4). Brains were removed, post-fixed in the same fixative (for 48 hr), and cut on a Vibratome in 50 μm coronal sections which were collected in PB until processing. Sections were incubated in 10% NDS (1 hr), followed by a solution containing rabbit polyclonal anti-cGLT-1a primary antibodies (3.0 μg/ml 2 hr at RT, and then overnight at 4°C). Polyclonal antibodies directed against a synthetic peptide corresponding to the rodent amino acid sequence 559-573 (SADCSVEEEPWKREK) of GLT-1a C terminus were used (characterized in Chen et al., 2004; Rothstein et al., 1994). Their specificity was demonstrated by the lack of immunoreactivity in GLT-1-KO mice (Chen et al., 2004; Omrani et al., 2009; Tanaka et al., 1997). Sections were rinsed and incubated first in 10% NBCS (15 min), and then in a solution containing donkey anti-rabbit Alexa 488 conjugated secondary antibodies (Jackson) (For details, see Melone et al., 2019). Sections were mounted, and coverslipped with propyl-gallate 0.1M in glycerol-PBS solution. The omission of the primary or secondary antibodies resulted in a lack of specific staining. Adjacent sections of those used for immunofluorescence were processed for Nissl staining.

Confocal microscopy

GLT-1a immunolabeled sections were examined with a Leica SP2 TCS-SL confocal microscope. For low magnification cortical fields containing layers I-II/III from primary somatosensory cortex, images were acquired as 512 × 512 pixel images (pixel size of 0.88 μm) with a HC PL Fluotar objective 20.0 × 0.50 dry (numerical aperture 0.50) and pinhole 2.3 Airy unit. To improve signal/noise ratio, 6 frames of each image were averaged. The acquisition of images was optimized through the "Q LUT" function which permitted direct visualization of pixel saturation. Photomultiplier gain was set so that the brightest pixel was just slightly below saturation, and the offset such that the darkest pixels were just above zero. Montage of final images was obtained by the alignment of single acquired cortical fields by Adobe Photoshop 21.0.1.

Pre-embedding electron microscopy

Mice were anesthetized with an intraperitoneal injection of chloral hydrate (300 mg/kg) and perfused transcardially with a flush of saline solution followed by 4% freshly depolymerized paraformaldehyde in 0.1 M phosphate buffer (PB; pH 7.4). Brains were removed, post-fixed in the same fixative (for 4 weeks) and cut on a Vibratome in 50 μm coronal sections which were collected in PB until processing (Melone et al., 2009). *Primary antibodies:* See above

Immunoperoxidase and pre-embedding procedure

Sections were treated with H_2O_2 (1% in PB; 30 min) to remove endogenous peroxidase activity, rinsed in PB and pre-incubated in 10% normal goat serum (NGS, 1 hr). Sections were then incubated in a solution containing GLT-1a antibodies (1.15 μg/ml; 2 h at room temperature [RT] and overnight at 4°C). The following day, sections were rinsed 3 times in PB and incubated first in 10% NGS (15 min) and then in a solution containing anti-rabbit biotinylated secondary antibodies (1:500; 1.5 hr at RT; Jackson ImmunoResearch Europe Inc.). Sections were subsequently rinsed in PB, incubated in avidin-biotin peroxidase complex (ABC Elite PK6100, Vector), washed several times in PB, and incubated in 3,3′diaminobenzidine tetrahydrochloride (DAB; 0.05% in 0.05 M Tris buffer, pH 7.6 with 0.03% H_2O_2). Method specificity was verified by substituting primary antibodies with PB or NGS. As previously described (Melone et al., 2009) after completion of immunoperoxidase procedure, sections were post-fixed in 1% osmium tetroxide in PB for 45 min and contrasted with 1% uranyl acetate in maleate buffer (pH 6.0; 1 h). After dehydration in ethanol and propylene oxide, sections were embedded in Epon/Spurr resin (Electron Microscopy Sciences, Hatfield, PA, USA), flattened between Aclar sheets (Electron Microscopy Sciences) and polymerized at 60°C for (48 hr). Chips including layers L1a and L2/3 of primary somatosensory cortex (SI) from

FHM2 and WT were selected by light-microscopic inspection, glued to blank epoxy and sectioned with an ultramicrotome (MTX; Research and Manufactoring Company Inc., Tucson, AZ, USA). The most superficial ultrathin sections (~60 nm) were collected and mounted on 200 mesh copper grids, stained with Sato's lead and examined with a Philips EM 208 and CM10 electron microscopes coupled to a MegaView-II high resolution CCD camera (Soft Imaging System). To minimize the effects of procedural variables, all material from FHM2 and WT for pre-embedding studies was processed in parallel.

QUANTIFICATION AND STATISTICAL ANALYSIS

Glutamatergic plumes

Image processing, regions of interest (ROI), and collection of fluorescence traces were performed in Fiji (Schindelin et al., 2012) using custom built and already available macros, while analysis of fluorescence traces were performed in MATLAB. Raw image stacks were converted to change in fluorescence ($\Delta F = F_t - F_0$), where F_t is the fluorescence intensity of a given frame and F_0 is the average fluorescence of the first 3 – 5 s of the trial (prior to whisker stimulation for *in vivo*). A band-pass filter (3 – 60 pixels) reduced noise artifacts and a maximum intensity projection (MIP) of the ΔF stack provided a spatial map of putative plumes for ROI generation (Figures 2A and S1). Circular ROIs were drawn around each plume with the diameter equal to the full width at half the maximum (FWHM) of the spatial pixel intensity profile in the MIP. All plumes were visually confirmed in the raw, unprocessed image stack series and only events with a diameter $\geq$ 3 pixels were further analyzed to prevent inclusion of noise artifacts. For *in vitro* one-photon (1P), analysis focused on 290 × 216.67 μm FOV in slices containing the barrel cortex and a ~550 μm^2 FOV containing hippocampal CA1. Bleach correction was required prior to generating the ΔF series and the initial 3 – 5 frames of each trial served as F_0. Fluorescence intensity traces were collected as the average intensity of all pixels within the ROI from the raw image stack (2P) or bleach corrected series (1P) following a 3D Gaussian blur to minimize noise (1 × 1 pixels x 0.4 frames) (Wang et al., 2019). Traces were than normalized as $\Delta F/F_0$ in MATLAB by dividing ΔF by the average fluorescence of the first 3 – 5 s of the imaging trail (F_0). For *in vivo* imaging, F_0 was the period prior to whisker stimulation. Plume characteristics were collected using the findpeaks function, where peak amplitude of plumes was the maximum $\Delta F/F_0$ and duration was the temporal FWHM of the peak amplitude. During high frequencies of plumes (veratridine, TFB-TBOA, KCl and SD) ROIs were drawn by hand because they could not be spatially segregated using the MIP.

Sensory glutamate

To generate ROIs for sensory glutamate responses, we first converted raw image stacks to ΔF using the same equation as described above for plumes, then generated a MIP for the entire series. The peak ΔF value for a single pixel in the MIP served as the maximum change in pixel intensity across the entire series. We converted the MIP to a binary image of all pixels with a ΔF value greater than 50% of the maximum change in pixel intensity (Theriot et al., 2012). This binary image served as our glutamate response map to generate ROIs because the response to whisker stimulation was consistently the largest amplitude fluorescence change across the imaging trial for epifluorescence. We also verified that ROIs avoided any major vessels or vessel shadows within the FOV. As described for plumes, traces were collected from raw images stacks following a 3D Gaussian blur to minimize noise (1 × 1 pixels x 0.4 frames), and converted to $\Delta F/F_0$ in MATLAB. A two-term exponential equation was fit to the decay of response (from peak to return to baseline) following a 40 ms stimulation in $\Delta F/F_0$ traces from individual trials to determine clearance kinetics (Figure 1C). Single-term equations systematically deviated from recordings during τ_{slow} in both genotypes and were considered a poor fit using an F-test for fit comparisons.

Recording during SD initiation

Basal glutamate fluorescence was measured as the mean pixel intensity within the induction port. The rise in basal fluorescence prior to SD used traces normalized ($\Delta F/F_0$) to the initial fluorescence during 0 μM veratridine and were fit with a polynomial from the start of the rise to SD induction or the first 10 min recording at 750 μM (see *In vivo* SD induction above). iGluSnFR expression was too low inside the fenestration for accurate recording in 2 mice (n = 1 WT and 1 FHM2), but sufficient in adjacent tissue within the field of view to determine SD induction. These mice were included in SD threshold analysis but excluded from plume and rise of glutamate fluorescence preceding SD. Plume rise was recorded as the concentration of veratridine that increased the relative frequency of plumes in an individual animal (Figure 5E). An additional two mice (n = 1 WT and 1 FHM2) did not have a rise in plume frequency prior to SD and, thus, were excluded from correlation with SD threshold. The amplitude and duration of the DC shift and glutamate during SD used the peak of the response and FWHM (Data S1). For SD induced with KCl in WT mice, all mice had a rise in plume frequency prior to SD initiation and were included in all analysis.

Recording during SD propagation

Analysis of plumes during SD propagation was as described above (Glutamatergic plumes section), with a few exceptions to better visualize plumes during SD propagation. To generate ROIs for plumes, we corrected for the decrease in basal glutamate fluorescence from the peak of the SD glutamate wave back to pre-SD fluorescence levels using a bleach correction plugin in Fiji. The bleach-corrected image stack was converted to change in fluorescence ($\Delta F = F_t - F_0$), where F_t is the fluorescence intensity of a given frame and F_0 is the average fluorescence of the first 5 s of the recording. Plumes were visually confirmed in the raw image stack, and traces were collected from the raw image stack following a 3D Gaussian blur (Wang et al., 2019). Plume characteristics were

collected in MATLAB using the findpeaks function, though the amplitude of plumes was defined as peak prominence (instead of maximum $\Delta F/F_0$) to adjust for amplitude of the SD wave itself, and the plume duration was the temporal full width at the half-maximum of the peak prominence. Plume latency was defined as the time (in seconds) from the end of the steepest rise in basal glutamate fluorescence during the SD wave to the peak prominence of an individual plume. The steepest rise in glutamate fluorescence during the SD wave typically ended at the peak amplitude of the SD, though in several FHM2 mice, a second slow rise in fluorescence occurred before reaching the true peak fluorescence of the wave.

In vivo laminar designation

L2/3 was distinguished from L1 based on the high density of neural somas in L2/3, which were silhouetted by iGluSnFR expression in the neuropil. Putative L1a was visualized as a decreased density in iGluSnFR expression relative to deeper L1b that resided near the surface of the brain. L1b consisted of the remaining region between L1a and L2/3. Additional sublamina likely exist within L1 (Nieuwenhuys, 2013; Vogt, 1991), though were not distinguishable in our data. In a small set of experiments with iGluSnFR and SR101 added to visualize astrocytes and the glial limtans, L1a typically overlapped with a band of parenchyma immediately below the glia limitans with few astrocyte somas (Figure S2; McCaslin et al., 2011). Neural Ca^{2+} plumes were recorded in the neuropil of the most superficial regions of L1 (putative L1a), and we verified no fluorescence somas were present in adjacent tissue using volume or 'Z stack' recordings.

EM data collection and analysis

All data were obtained from a region of the mouse parietal cortex characterized by the presence of a conspicuous layer IV with intermingled dysgranular regions, densely packed layers II and III, and a relatively cell-free layer Va. This area corresponds to primary somatosensory (S1) cortex (Chapin and Lin, 1990). GLT-1a profiles were studied in ultrathin sections from the surface of the embedded blocks. Quantitative data derived from the analysis of microscopic fields of cortical neuropil (10–15 ultrathin sections/animal) selected and captured at original magnifications of 12,000x-30,000x. Sampling from L1a was carried out within 30-35 μm from the cortical surface. Microscopical fields from FHM2 and WT containing GLT-1a positive processes were randomly selected. Acquisition of microscopical fields and analysis of FHM2 and WT mice were performed in a blind manner. For the identification of GLT-1a negative synapses and of GLT-1a localization at asymmetric synapses (in the case of GLT-1a positive synapses), subcellular elements contributing to synapses were classified according to well-established criteria (e.g., DeFelipe et al., 1999; Peters et al., 1991). Briefly, the presynaptic terminal was characterized by clear and round vesicles nearby the presynaptic density, the synaptic cleft displayed electrodense material, the pre- and postsynaptic membranes defining the active zone and the postsynaptic specialization were characterized by electron densities, and finally the prominent postsynaptic density permitted to identify the asymmetric synapses (e.g., DeFelipe et al., 1999). Astrocytic processes in close relationship with synapses were identified by their typical irregular outlines and the paucity of cytoplasmic components (with the exception of ribosomes, glycogen granules and various fibrils; Peters et al., 1991). A synapse was considered GLT-1a negative when none of all synaptic domains exhibited GLT-1a immunoreactivity (i.e., axon terminal, postsynaptic dendrite, and astrocytic processes lying on pre- and/or postsynaptic elements). Interestingly, virtually all GLT-1a negative synapses were not touched by astrocytic processes confirming that almost all astrocytes and their processes do express GLT-1a immunoreactivity (de Vivo et al., 2010). A synapse was considered GLT-1a positive when GLT-1a immunoreactivity (ir) was localized at axon terminals and/or at astrocytic processes touching pre- and/or postsynaptic elements in any part of their perimeter (thus including also astrocytic processes relatively far from the active zone/postsynaptic density complex [AZ/PSD]). To gather data on the relationship between GLT-1a positive astrocytic processes and asymmetric synapses, distances between each edge of AZ/PSD complexes and the closest point of GLT-1a positive astrocytic processes were estimated by ImageJ (Schneider et al., 2012) passing along the membrane of profiles. Measures were collected, and the frequency distribution of distances was determined using wide sectors of 100 nm. According to previous studies, any distance $\leq$ of 300 nm and $>$ of 300 nm was considered perisynaptic and extrasynaptic, respectively (Barthó et al., 2004; Lujan et al., 1996; Melone et al., 2009, 2011, 2015, 2019).

Statistics

Selection of statistical tests and data visualizations were based on the distribution of a given dataset, determined using an Anderson-Darling test (e.g., bar-graph and t test for parametric versus box-whisker plot and Wilcoxon rank sum for non-parametric). Statistical analyses were performed using MATLAB and GraphPad Prism Software. Descriptions of tests used and n are located in the figure legends. A list of means/medians and standard error of all datasets is included in Data S1. Data are reported as grand mean ± SEM unless otherwise stipulated. All bar graphs represent the grand mean with error bars representing the SEM. All box-whisker plots represent the median (black horizontal line), IQR ('box') and 1.5*IQR ('whisker'). Data points beyond 1.5*IQR are represented as '+'.